

# Refining the WASP-132 multi-planetary system: discovery of a cold giant planet and mass measurement of a hot super-Earth

Nolan Grieves<sup>1,\*</sup>, François Bouchy<sup>1</sup>, David J. Armstrong<sup>2,3</sup>, Babatunde Akintanmi<sup>1</sup>, Angelica Psaridi<sup>1</sup>, Solène Ulmer-Moll<sup>1,4</sup>, Yolanda G. C. Frensch<sup>1</sup>, Ravit Helled<sup>5</sup>, Simon Müller<sup>5</sup>, Henrik Knierim<sup>5</sup>, Nuno C. Santos<sup>6,7</sup>, Vardan Adibekyan<sup>6</sup>, Léna Parc<sup>1</sup>, Matthew P. Battley<sup>1</sup>, Nicolas Unger<sup>1</sup>, Guillaume Chaverot<sup>1</sup>, Daniel Bayliss<sup>2,3</sup>, Xavier Dumusque<sup>1</sup>, Faith Hawthorn<sup>2,3</sup>, Pedro Figueira<sup>1,6</sup>, Marcelo Aron Fetzner Keniger<sup>2,3</sup>, Jorge Lillo-Box<sup>8</sup>, Louise Dyregaard Nielsen<sup>9,1</sup>, Ares Osborn<sup>2,3</sup>, Sérgio G. Sousa<sup>6</sup>, Paul Strøm<sup>2,3</sup>, and Stéphane Udry<sup>1</sup>

<sup>1</sup> Observatoire de Genève, Université de Genève, 51 Chemin Pegasi, 1290 Versoix, Switzerland

<sup>2</sup> Department of Physics, University of Warwick, Gibbet Hill Road, Coventry, UK

<sup>3</sup> Center for Exoplanets and Habitability, University of Warwick, Gibbet Hill Road, Coventry, UK

<sup>4</sup> Physikalisches Institut, University of Bern, Gesellschaftsstrasse 6, 3012 Bern, Switzerland

<sup>5</sup> Center for Theoretical Astrophysics & Cosmology, Institute for Computational Science, University of Zurich, Zürich, Switzerland

<sup>6</sup> Instituto de Astrofísica e Ciências do Espaço, Universidade do Porto, CAUP, Rua das Estrelas, 4150-762 Porto, Portugal

<sup>7</sup> Dep. de Física e Astronomia, Faculdade de Ciências, Universidade do Porto, Rua do Campo Alegre, 4169-007 Porto, Portugal

<sup>8</sup> Centro de Astrobiología (CAB), CSIC-INTA, Dep. de Astrofísica, ESAC campus, 28692, Villanueva de la Cañada (Madrid), Spain

<sup>9</sup> European Southern Observatory, Karl-Schwarzschild-Strasse 3, 85748 Garching, Germany

Received 6 October 2023; accepted XXX

## ABSTRACT

Hot Jupiters generally do not have nearby planet companions, as they may have cleared out other planets during their inward migration from more distant orbits. This gives evidence that hot Jupiters more often migrate inward via high-eccentricity migration due to dynamical interactions between planets rather than more dynamically cool migration mechanisms through the protoplanetary disk. Here we further refine the unique system of WASP-132 by characterizing the mass of the recently validated 1.0-day period super-Earth WASP-132 c (TOI-822.02) interior to the 7.1-day period hot Jupiter WASP-132 b. Additionally, we announce the discovery of a giant planet at a 5-year period (2.7 AU). We also detect a long-term trend in the radial velocity data indicative of another outer companion. Using over nine years of CORALIE RVs and over two months of highly-sampled HARPS RVs, we determine the masses of the planets from smallest to largest orbital period to be  $M_c = 6.26^{+1.84}_{-1.83} M_\oplus$ ,  $M_b = 0.428^{+0.015}_{-0.015} M_{\text{Jup}}$ , and  $M_d \sin i = 5.16^{+0.52}_{-0.52} M_{\text{Jup}}$ , respectively. Using TESS and CHEOPS photometry data we measure the radii of the two inner transiting planets to be  $1.841^{+0.094}_{-0.093} R_\oplus$  and  $0.901^{+0.038}_{-0.038} R_{\text{Jup}}$ . WASP-132 is a unique multi-planetary system in that both an inner rocky planet and an outer giant planet are in a system with a hot Jupiter. This suggests it migrated via a more rare dynamically cool mechanism and helps to further our understanding of how hot Jupiter systems may form and evolve.

**Key words.** planets and satellites: detection, dynamical evolution and stability, fundamental parameters

## 1. Introduction

Some previous studies found that most hot Jupiters do not have nearby planet companions. This was based on nondetections of additional planets in radial velocity (RV) data (e.g., Wright et al. 2009) and photometry data by looking for both additional transit signals (e.g., Steffen et al. 2012; Huang et al. 2016; Hord et al. 2021) and transit timing variations (e.g., Steffen et al. 2012; Wang et al. 2021; Ivshina & Winn 2022). The lack of detected planets may be a result of highly eccentric giant planets clearing out any low-mass inner planets in the system during their migration inward (Mustill et al. 2015). These results suggest that high-eccentricity migration due to dynamical interactions between planets (e.g., Rasio & Ford 1996; Weidenschilling & Marzari 1996; Lin & Ida 1997) may be a more common migration mechanism for gas giant planets compared to disk-driven migration (e.g., Goldreich & Tremaine 1980; Ward 1997; Baruteau et al. 2014).

However, Wu et al. (2023) recently searched for transit timing variations across the full four-year Kepler (Borucki et al. 2010) data set and found that at least  $12 \pm 6\%$  of hot Jupiters have a nearby companion. Continued surveys and recent advancements in the precision of both photometry and RV observations have allowed the detection of some of these companions including WASP-47 (Becker et al. 2015), Kepler-730 (Zhu et al. 2018; Cañas et al. 2019), TOI-1130 (Huang et al. 2020), WASP-148 (Hébrard et al. 2020), WASP-132 (Hord et al. 2022), and TOI-2000 (Sha et al. 2022). These companions give strong evidence that these hot Jupiters migrated via quiescent mechanisms that are dynamically cool and allow nearby planetary companions to remain in the system.

Giant long-period planets have also been detected in systems with small close-in planets (e.g., Santos et al. 2016). Several studies have worked to determine the occurrence of long-period ( $\geq 1$  year) giant ( $M_p \geq 0.3 M_{\text{Jup}}/95 M_\oplus$ ;  $R_p \geq 0.45 R_{\text{Jup}}/5 R_\oplus$ ) planets, also known as cold Jupiters, in systems that contain close-in ( $\lesssim 100$  days) small ( $R_p \lesssim 4 R_\oplus$ ;  $M_p \lesssim 30 M_\oplus$ ) planets.

\* e-mail: nolangrieves@gmail.com

These studies have varying results with some suggesting a positive correlation between close-in small planets and cold Jupiters (e.g., Zhu & Wu 2018; Bryan et al. 2019; Herman et al. 2019; Rosenthal et al. 2022) while others find a negative correlation (e.g., Barbato et al. 2018; Bonomo et al. 2023). A positive correlation suggests that these two planet populations do not directly compete for solid material (e.g., Zhu & Wu 2018). However, multiple theories suggest a negative correlation including that the early formation of a cold Jupiter may prevent the nuclei of smaller planets from migrating inward (e.g., Izidoro et al. 2015), or that cold Jupiters may reduce the flux of material required to form close-in planets larger than Earth (e.g., Lambrechts et al. 2019). Recently Zhu (2023) looked at the metallicity dimension of the super Earth vs cold Jupiter correlation and found that there is a positive correlation between the two around metal-rich host stars; however, a correlation is unclear for metal-poor host stars due to limited sample size.

Here we analyze the unique WASP-132 planetary system. WASP-132 b was first discovered by Hellier et al. (2017) who measured the planet to have a 7.1 day period,  $0.41 \pm 0.03 M_{\text{Jup}}$  mass, and  $0.87 \pm 0.03 R_{\text{Jup}}$  radius using 23,300 WASP-South (Pollacco et al. 2006) observations from 2006 May - 2012 June, 36 1.2-m Euler/CORALIE (Queloz et al. 2001) RVs from 2014 March - 2016 March, and TRAPPIST (Jehin et al. 2011) photometry data on 2014 May 05. Hord et al. (2022) then later announced the discovery and validation of an inner 1.01 day  $1.85 R_{\oplus}$  planet using data from the Transiting Exoplanet Survey Satellite (TESS; Ricker et al. 2015), but did not characterize the mass. Here we use new RV measurements to characterize the mass of the previously discovered super-Earth WASP-132 c (Hord et al. 2022). We also announce the discovery of a long-period massive giant planet and update all bulk measurements of the system. In Section 2 we present the observations used in this work. In Section 3 we describe our analysis and results. We discuss our results in Section 4 and finally give our conclusions Section 5.

## 2. Observations

### 2.1. Photometry

#### 2.1.1. TESS

As detailed in Hord et al. (2022), WASP-132 (TOI-822, TIC 127530399) was observed by TESS in Sector 11 from UT 2019 April 23 to May 20 (23.96 days) in CCD 2 of Camera 1 and in Sector 38 from UT 2021 April 29 to May 26 (26.34 days) in CCD 1 of Camera 1. Data for WASP-132 were collected at 2-minute cadence in Sectors 11 and 38 and at 20-second cadence in Sector 38. The data were processed by the TESS Science Processing Operation Center (SPOC) pipeline (Jenkins et al. 2016) and were searched by the Transiting Planet Search module (TPS; Jenkins 2002; Jenkins et al. 2010). The TPS recovered WASP-132 b and WASP-132 c with a period of 1.01153 days with a signal-to-noise ratio (S/N) of 10.6 in the combined data from the two sectors.

Hord et al. (2022) searched and analyzed the TESS light curves using the Presearch Data Conditioning Simple Aperture Photometry (PDC\_SAP) TESS light curves generated by the TESS SPOC pipeline (Smith et al. 2012; Stumpe et al. 2012, 2014) at the 2-minute cadence for TESS Sectors 11 and 38. Using the transit least-squares (TLS) search algorithm (Hippke & Heller 2019), Hord et al. (2022) recovered the hot Jupiter WASP-132 b signal as well as the WASP-132 c signal with a period

( $1.0119 \pm 0.0032$  days), depth, and mid-transit time consistent with the values reported by the SPOC pipeline. Hord et al. (2022) also further established the planetary nature of the WASP-132 c signal by using the validation tools *vespa* (Morton 2012, 2015) and TRICERATOPS (Giacalone & Dressing 2020; Giacalone et al. 2021) on the signal and found false-positive probabilities of  $9.02 \times 10^{-5}$  and 0.0107, respectively.

WASP-132 was recently observed again by TESS in Sector 65 from UT 2023 May 4 to 2023 May 29. Data for WASP-132 were collected at 2-minute cadence in Sector 65. We run an independent analysis of the TESS data, now including Sector 65 and use the PDC\_SAP TESS light curves generated by the TESS SPOC pipeline at 2-minute cadence for all three sectors. The full TESS light curves are displayed in Figure A.1.

#### 2.1.2. CHEOPS

We observed three transits of WASP-132 c with the European Space Agency CHARacterizing ExOPlanets Satellite (CHEOPS; Broeg et al. 2013; Benz et al. 2021). CHEOPS is a space telescope with a 32 cm aperture for the purpose of precision follow-up of known planetary systems. We observed transits of WASP-132 c with CHEOPS on 19 May 2022, 4 June 2022, and 11 June 2022 (Program ID: PR430010, PI: B. Akisanmi) with an exposure time of 60 seconds. The CHEOPS photometry was processed using the dedicated data reduction pipeline (version 13.1; Hoyer et al. 2020). To identify and correct for systematics affecting CHEOPS light curves, we decorrelate the data against the temporal evolution of the telescope roll angle and the flux of background stars inside the photometric aperture (see e.g., Bonfanti et al. 2021). We discuss the removal of systematics in our CHEOPS data in Section 3.3. The CHEOPS light curves are displayed in Figure A.2. A table of the reduced CHEOPS photometric observations is available in a machine-readable format at the CDS.

### 2.2. Spectroscopy

#### 2.2.1. CORALIE

In addition to the 36 RV measurements published by Hellier et al. (2017) and used by Hord et al. (2022), we obtained 37 more CORALIE RVs for a total of 73 CORALIE observations taken across a time span of over nine years. The CORALIE spectrograph is on the Swiss 1.2 m Euler telescope at La Silla Observatory, Chile (Queloz et al. 2001) and has a resolution of  $R \sim 60,000$ .

The CORALIE spectrograph began observations in June 1998 and went through two significant upgrades in June 2007 and in November 2014 in order to increase the overall efficiency and accuracy of the instrument. The 2007 upgrade replaced CORALIE's fiber link and cross-disperser optics (Ségransan et al. 2010). The 2014 upgrade replaced CORALIE's fiber link with octagonal fibers (Chazelas et al. 2012) and added a Fabry-Pérot calibration unit (Cersullo et al. 2017). Both interventions on the instrument introduced small offsets between the RV measurements collected before and after each upgrade, depending on such parameters as the spectral type and systemic velocity of the observed star.

Observations of WASP-132 with CORALIE began in March 2014 and we have 22 observations with the first upgrade (the "COR07" setup) and 51 observations after the November 2014 upgrade with the "COR14" setup. We treat these two data sets as separate instruments to account for any offsets in the mea-

surements. We reduced the spectra with the standard calibration reduction pipeline and computed RVs by cross-correlating with a binary G2 mask (Pepe et al. 2002). We obtained typical RV uncertainties of  $\sim 21 \text{ m s}^{-1}$  for our CORALIE RVs. The CORALIE RVs are displayed in Figure 1. The CORALIE RVs are presented in tables A.1 and A.2 and are available in a machine-readable format at the CDS.

### 2.2.2. HARPS

After the announcement of an inner planet candidate to the hot Jupiter in the WASP-132 system, we began observing WASP-132 with the HARPS spectrograph (Pepe et al. 2002; Mayor et al. 2003) to obtain more precise RV measurements and measure the mass of the inner 1-day period planet. HARPS is hosted by the ESO 3.6-m telescope at La Silla Observatory, Chile and has a resolving power of  $R \sim 115,000$ .

We obtained 48 HARPS observations of WASP-132 from 17 January 2022 to 1 April 2022 as part of the NOMADS program (PI Armstrong, 108.21YY.001). The HARPS raw data were reduced according to the standard HARPS data reduction software pipeline<sup>1</sup> with a spectral-type K5 binary mask. We obtained typical RV uncertainties of  $\sim 2.2 \text{ m s}^{-1}$  for our HARPS RVs. Bisector span and full width at half-maximum (FWHM) of the cross-correlation function (CCF) and other line-profile diagnostics were computed as well. The HARPS spectra were also used to derive spectral parameters for WASP-132, as detailed in Section 3.1. The HARPS RVs are displayed in Figure 1. Figure 1 also displays a two-planet Keplerian model (see Section 3.2.2) for both the CORALIE and HARPS RVs. The HARPS RVs are presented in table A.3 and are available in a machine-readable format at the CDS.

## 3. Analysis and results

### 3.1. Host Star Parameters

Hord et al. (2022) compared several methods to determine the host star parameters of WASP-132 including those reported by Hellier et al. (2017), the TICv8.2 values (Stassun et al. 2018, 2019), an isochrone-based analysis using *isoclassify* (Huber et al. 2017; Berger et al. 2020), as well as two different broadband Spectral Energy Distribution (SED) plus parallax analyses. Hord et al. (2022) found these methods to be consistent and adopted the isochrone analysis as their final parameters which used spectroscopic  $T_{\text{eff}}$  and metallicity from Hellier et al. (2017), Gaia Data Release 2 (DR2; Gaia Collaboration et al. 2016a; Bailer-Jones et al. 2018; Gaia Collaboration et al. 2018a) parallax and coordinates, the Two Micron All-Sky Survey (2MASS; Skrutskie et al. 2006)  $K_S$  magnitude, and a photometric extinction estimated from Bovy et al. (2016) as inputs.

The spectroscopic  $T_{\text{eff}}$  and [Fe/H] from Hellier et al. (2017) that Hord et al. (2022) used as inputs for their final model were determined using only 36 CORALIE spectra. We now have 48 higher resolution HARPS spectra and can derive higher precision spectral parameters using a combined HARPS spectrum. The stellar atmospheric parameters ( $T_{\text{eff}}$ ,  $\log g$ , microturbulence and [Fe/H]) were derived using the methodology described in Sousa (2014); Santos et al. (2013). We first measured the equivalent widths (EWs) of 224 FeI and 35 FeII lines using the ARES v2 code<sup>2</sup> (Sousa et al. 2015). Then we used these EWs together

**Table 1.** Stellar parameters of WASP-132.

Parameter	Value	Source
<u>Identifying Information</u>		
TESS ID	TIC 127530399	TESS
TOI ID	TOI-822	TESS
2MASS ID	2MASS J14302619-4609330	2MASS
Gaia ID	6099012478412247296	Gaia DR3
<u>Astrometric parameters</u>		
R.A. (J2000, h:m:s)	14:30:26.21	TICv8
Dec (J2000, h:m:s)	-46:09:34.26	TICv8
Parallax (mas)	$8.092 \pm 0.019$	Gaia DR3
Distance (pc)	$123.17 \pm 0.57$	3.1
<u>Photometric parameters</u>		
B	$13.142 \pm 0.011$	APASS
V	$11.938 \pm 0.046$	APASS
G	$11.747 \pm 0.020$	Gaia DR3
$B_p$	$12.300 \pm 0.020$	Gaia DR3
$R_p$	$11.049 \pm 0.020$	Gaia DR3
J	$10.257 \pm 0.026$	2MASS
H	$9.745 \pm 0.023$	2MASS
$K_S$	$9.674 \pm 0.024$	2MASS
W1	$9.557 \pm 0.022$	WISE
W2	$9.638 \pm 0.020$	WISE
W3	$9.575 \pm 0.040$	WISE
$A_V$	$0.114 \pm 0.11$	Sect. 3.1
<u>Bulk parameters</u>		
$T_{\text{eff}}$ (K)	$4686 \pm 99$	Sect. 3.1
[Fe/H]	$0.15 \pm 0.05$	Sect. 3.1
[Mg/H]	$0.13 \pm 0.09$	Sect. 3.1
[Si/H]	$0.27 \pm 0.11$	Sect. 3.1
$\log g_*$ ( $\text{cm s}^{-2}$ )	$4.56 \pm 0.03$	Sect. 3.1
Spectral type	K4V	Sect. 3.1
Mass ( $M_{\odot}$ )	$0.789 \pm 0.039$	Sect. 3.1
Radius ( $R_{\odot}$ )	$0.758 \pm 0.032$	Sect. 3.1
$\rho_*$ ( $\text{g cm}^{-3}$ )	$2.56^{+0.21}_{-0.18}$	Sect. 3.1
Luminosity ( $L_{\odot}$ )	$0.266^{+0.017}_{-0.012}$	Sect. 3.1
Age (Gyrs)	$7.2^{+4.3}_{-4.4}$	Sect. 3.1
$\log(R'_{\text{HK}})$	$-4.852 \pm 0.039$	Sect. 3.1
$v \sin i$ ( $\text{km s}^{-1}$ )	$3.3 \pm 0.6$	Sect. 3.1

with a grid of Kurucz model atmospheres (Kurucz 1993) and the radiative transfer code MOOG (Snedden 1973) to determine the parameters under assumption of ionization and excitation equilibrium. The abundances of Mg and Si were also derived using the same tools and models as detailed in (e.g. Adibekyan et al. 2012, 2015). Although the EWs of the spectral lines were automatically measured with ARES, we performed careful visual inspection of the EWs measurements as only three lines are available for the Mg abundance determination. Using the combined HARPS spectrum we find a  $T_{\text{eff}} = 4686 \pm 99$ , [Fe/H] =  $+0.15 \pm 0.05$ , and  $\log g_* = 4.55 \pm 0.29$ . We find the star to be a K4V spectral type from its  $T_{\text{eff}}$  value using the updated table from Pecaut & Mamajek (2013)<sup>3</sup>.

We derived a rotational projected velocity of  $v \sin i = 3.3 \pm 0.6 \text{ km s}^{-1}$  by performing spectral synthesis with MOOG on 36 iron

<sup>1</sup> [Is.eso.org/sci/facilities/lasilla/instruments/harps/doc/index.html](https://www.eso.org/sci/facilities/lasilla/instruments/harps/doc/index.html)

<sup>2</sup> The last version of ARES code (ARES v2) can be downloaded at <http://www.astro.up.pt/~sousasag/ares>

<sup>3</sup> [https://www.pas.rochester.edu/~emamajek/EEM\\_dwarf\\_UBVJHK\\_colors\\_Teff.txt](https://www.pas.rochester.edu/~emamajek/EEM_dwarf_UBVJHK_colors_Teff.txt)

isolated lines and by fixing the stellar parameters, macroturbulent velocity, and limb-darkening coefficient (Costa Silva et al. 2020). The linear limb-darkening coefficient (0.7) was determined using ExoCTK package (Bourque et al. 2021) considering the stellar parameters. We note that a  $v \sin i = 3.3 \pm 0.6 \text{ km s}^{-1}$  yields a  $P_{\text{rot}}/\sin i = 11.35 \pm 2.09$  days (with the  $R_*$  value derived below); however, this is not in agreement with the  $v \sin i = 0.9 \pm 0.8 \text{ km s}^{-1}$  Hellier et al. (2017) derived with CORALIE spectra nor with the  $33 \pm 3$  day signal from a possible rotational modulation in the WASP data. Given that WASP-132 is a cooler star the Doyle et al. (2014) calibrations are not valid, a macroturbulent velocity of  $2 \text{ km s}^{-1}$  was assumed and the  $v \sin i$  value can vary with this assumption.

To derive our final stellar parameters we fit the SED of each star, using the MESA Isochrones and Stellar Tracks (MIST) (Dotter 2016; Choi et al. 2016) via the IDL suite EXOFASTv2 (Eastman et al. 2019). The stellar parameters are simultaneously constrained by the SED and the MIST isochrones with this method as the SED primarily constrains the stellar radius  $R_*$  and effective temperature  $T_{\text{eff}}$ , while a penalty for straying from the MIST evolutionary tracks ensures that the resulting star is physical in nature (see Eastman et al. (2019), for more details on the method).

We use the  $T_{\text{eff}}$ ,  $\log g_*$ , and  $[\text{Fe}/\text{H}]$  values along with their uncertainties from the HARPS spectral analysis as priors for our stellar model and the extinction ( $A_V$ ) is limited to the maximum line-of-sight extinction from the Galactic dust maps of Schlafly & Finkbeiner (2011). We put a Gaussian prior for parallax from the value and uncertainty in *Gaia* DR3 (Gaia Collaboration et al. 2021). We note the *Gaia* DR3 parallax (8.09240) was corrected by subtracting  $-0.02705$  mas according to the Lindegren et al. (2021) prescription. For the SED fit we use photometry from APASS DR9  $B_V$  (Henden et al. 2016); *Gaia* DR3  $G$ ,  $B_P$ , and  $R_P$  (Gaia Collaboration et al. 2021); 2MASS  $J$ ,  $H$ , and  $K_S$  (Skrutskie et al. 2006); and ALL-WISE  $W1$ ,  $W2$ , and  $W3$  (Wright et al. 2010), which are presented in Table 1.

We also use the HARPS spectra to estimate the  $\log(R'_{\text{HK}})$  of WASP-132 with the method described by Gomes da Silva et al. (2021) using the bolometric correction by Suárez Mascareño et al. (2015) and find a  $\log(R'_{\text{HK}}) = -4.852 \pm 0.039$ , which suggests that WASP-132 is only a moderately chromospherically active or inactive star (e.g., Henry et al. 1996). From this  $\log(R'_{\text{HK}})$  value we obtain a chromospheric rotational period via the relation by Noyes et al. (1984) and Mamajek & Hillenbrand (2008) to be  $44 \pm 8$  days which is closer to the  $33 \pm 3$  day estimate by Hellier et al. (2017) from photometry variation than our estimate from  $v \sin i$ .

We present our final stellar parameters in Table 1. The  $T_{\text{eff}}$  and  $[\text{Fe}/\text{H}]$  values are from the HARPS spectral analysis, while the  $\log g_*$ ,  $A_V$ , stellar mass, age, density, and luminosity are outputs of the EXOFASTv2 fit. Overall, we find our stellar parameters including mass and radius to be close in value and within uncertainties of those presented by Hord et al. (2022).

## 3.2. Initial RV Analysis

### 3.2.1. Rossiter McLaughlin Effect

The Rossiter-McLaughlin effect (Rossiter 1924; McLaughlin 1924) occurs during a planetary transit and impacts RVs from a typical Keplerian motion. We estimated the expected RV amplitude of the Rossiter-McLaughlin effect for both transiting planets with the classical method (Eq. 40 from Winn 2010) using our expected  $v \sin i$  and stellar radius measurements along

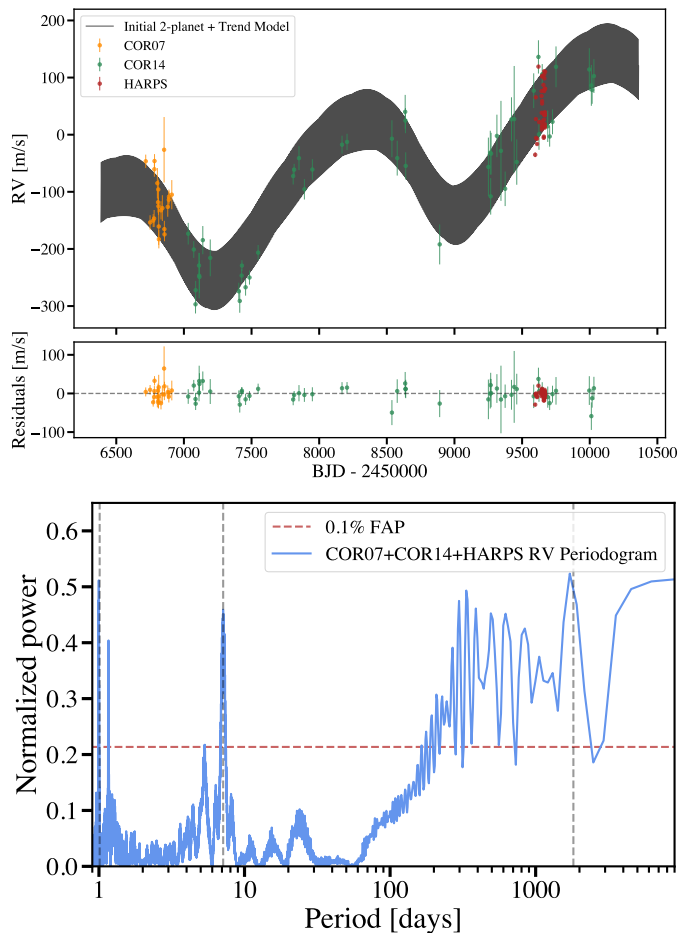


**Fig. 1.** *Top:* WASP-132 CORALIE and HARPS RVs with a two-planet (excluding the 1-day planet) Keplerian model plus a linear trend as described in Section 3.2.2. *Bottom:* GLS periodogram of the original CORALIE and HARPS RVs. The vertical gray dashed lines display the planet periods presented in Section 3.3.

with our derived values of the planets' radii and impact parameters, which we later describe in Section 3.3. We find Rossiter-McLaughlin effect RV amplitudes of  $\sim 1.55 \text{ m s}^{-1}$  for planet c and  $\sim 47.36 \text{ m s}^{-1}$  for planet b. Thus it is necessary to remove RV data that occurred during transits to not affect the RV model parameters. Using the period and transit duration that we later describe in Section 3.3, we find three CORALIE RVs and four HARPS RVs that occur during a transit of planet c. We removed the four HARPS RVs from our analysis, but given the relatively small impact the planet c Rossiter-McLaughlin effect will have on CORALIE data we did not remove the three CORALIE RVs. We also find one CORALIE RV and five HARPS RVs that are during a transit of planet b and we remove all of these data from our analysis. The RVs that occur during a planet transit are noted in Appendix Tables A.1, A.2, and A.3. We note that high resolution ESPRESSO (Pepe et al. 2021) observations of the Rossiter-McLaughlin signal for both planets were obtained and are in preparation for publication by a separate team.

### 3.2.2. HARPS two-planet residuals analysis

Our CORALIE and HARPS RVs clearly show the signal of the 7-day hot Jupiter and a longer period companion around 1800 days as seen in the generalized Lomb-Scargle (GLS) pe-

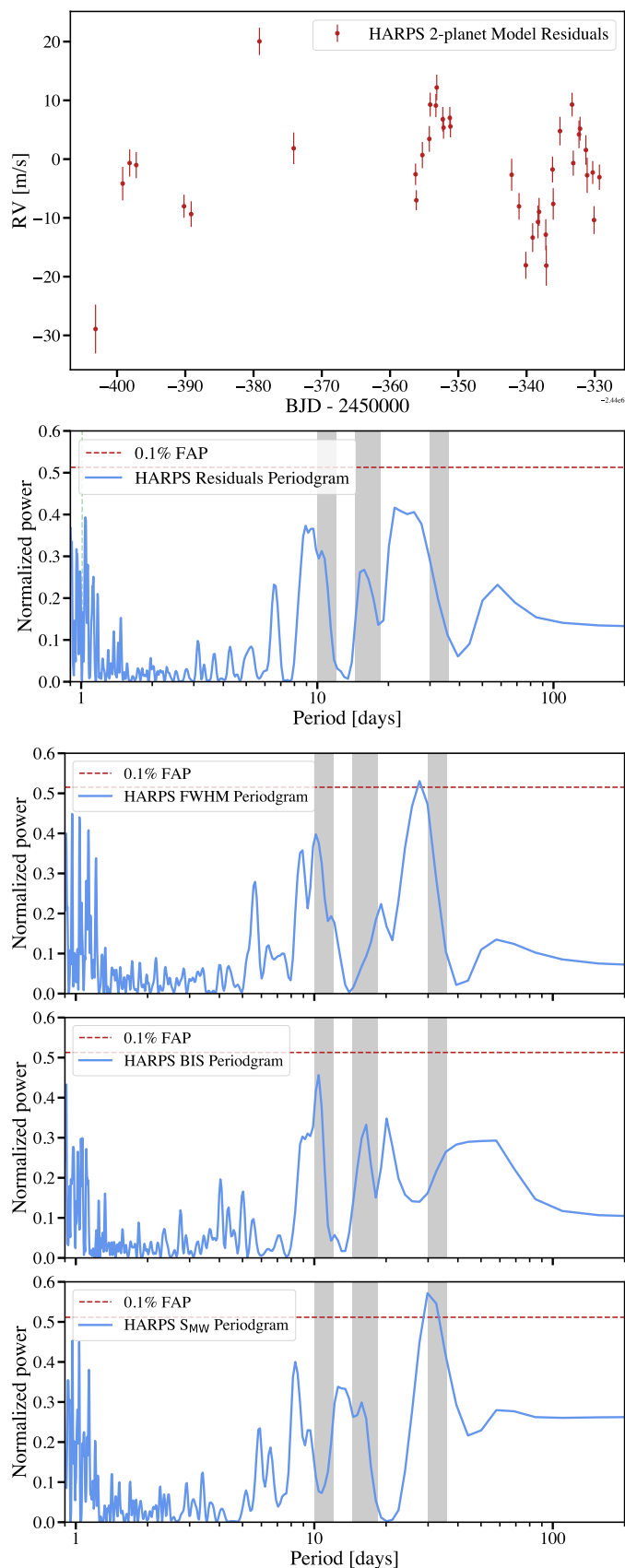


**Fig. 2.** *Top:* HARPS RV residuals after fitting CORALIE and HARPS data with a two-planet plus trend model and its corresponding and GLS periodogram. *Bottom:* GLS periodograms for the HARPS data activity indicators CCF FWHM, CCF BIS, and Mt Wilson ‘S index’  $S_{MW}$  from top to bottom respectively. The gray vertical bands show the possible rotation period  $P_{rot} = 33 \pm 3$  days and harmonics  $P_{rot}/2$  and  $P_{rot}/3$ .

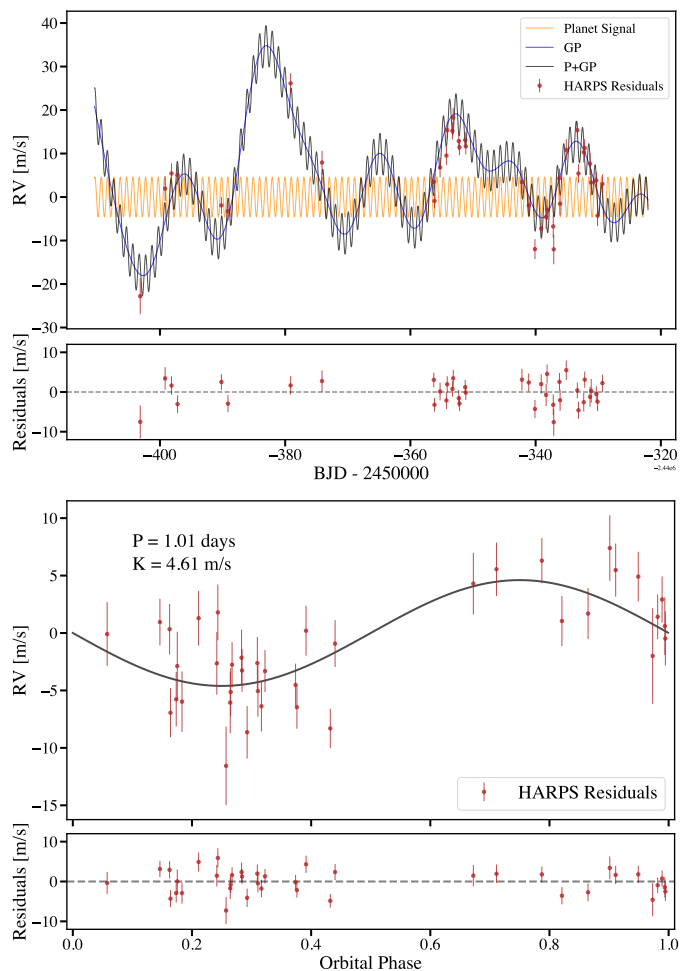


**Fig. 3.** *Top:* HARPS RV residuals after fitting CORALIE and HARPS data with a two-planet plus trend model described in Section 3.2.2 with a 1-planet Keplerian plus GP model constrained by the HARPS RV and BIS. *Bottom:* HARPS RV residuals from the top phased to the 1-day planet model.

riodogram (Lomb 1976; Scargle 1982; Zechmeister & Kürster 2009) implemented in the *astropy* (Astropy Collaboration et al. 2013, 2018) Python package of all the WASP-132 RVs in Figure 1. The *astropy* periodogram package can calculate False Alarm Probabilities (FAP) using various methods and we use the default Baluev (2008) method. Notably, we see the 7-day and long-period companion as well as one-day signals above the 0.1% FAP level in the periodogram. We also detected that a long-term RV trend is within the data.

In order to detect the much smaller signal from the 1-day period super-Earth planet we first fit the longer period signals and analyzed the residuals. For our initial RV analysis, we used the software suite *pyaneti*<sup>4</sup> (Barragán et al. 2019, 2022), which couples a Bayesian framework with a Markov chain Monte Carlo (MCMC) sampling to produce posterior distributions of the fitted parameters. We first fit the RVs with two Keplerians for the hot Jupiter and long-period outer companion as well as a linear trend. We note that we fit the data without a linear trend and the linear trend model is preferred with a difference in Bayesian Information Criterion (BIC) of 134. We put Gaussian priors on the period of the hot Jupiter based on our transit analysis presented in Section 3.3. With our initial two-planet

<sup>4</sup> <https://github.com/oscaribv/pyaneti>

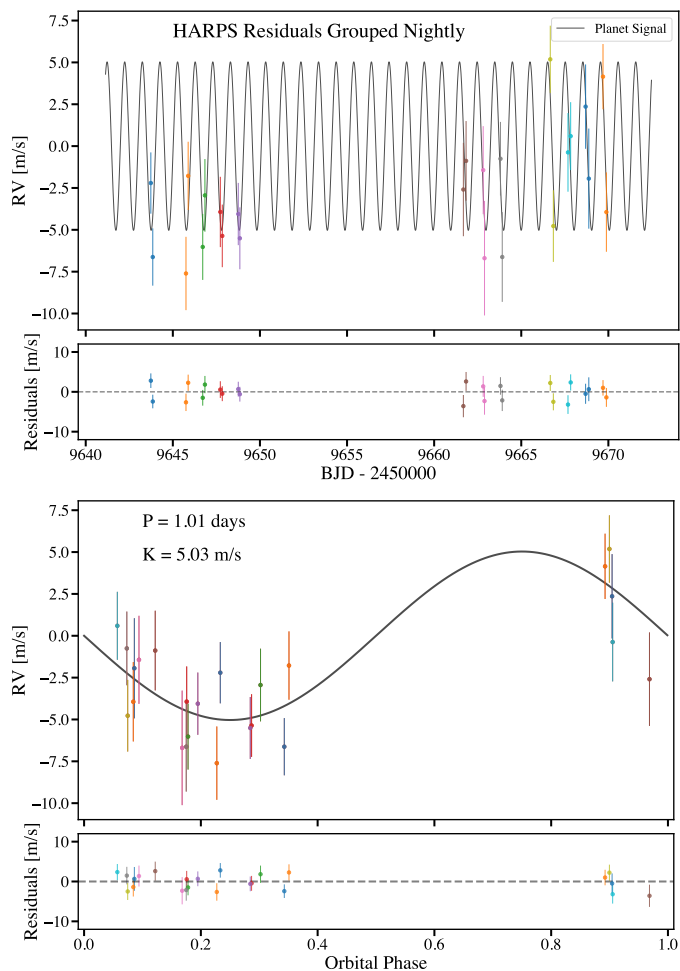


**Fig. 4.** HARPS RV residuals after fitting CORALIE and HARPS data with a two-planet plus trend model described in Section 3.2.2. Here we only include HARPS data that had two observations in one night for a total of 12 nights. We then fit a single Keplerian model with each night treated as different instrument with its own offset. Each night is shown with different colors. We show the phased RV plot in the bottom.

fit we find the outer companion to have a period of 1792 days and RV semi-amplitude  $K = 105.6 \text{ m s}^{-1}$  and a linear trend of  $23.5^{+2.4}_{-2.6} \text{ m s}^{-1} \text{ year}^{-1}$ . After removing these signals we analyzed the HARPS RVs which have the necessary precision to detect the smaller 1-day planet.

Noticeably the HARPS RV residuals of the 2-planet plus trend fit have variation much larger than the expected signal from the 1-day period super-Earth planet and we find strong signals at  $\sim 21$  and  $\sim 10$  days as displayed in Figure 2. It is well known that magnetically active regions (spots and plages) can induce periodic and quasi-periodic Doppler signals at the stellar rotation frequency and its harmonics (e.g., Boisse et al. 2011). Our  $\log(R'_{\text{HK}}) = -4.852 \pm 0.039$  value suggests that the star may be magnetically active and additionally Hellier et al. (2017) found a possible rotational modulation with a period of  $33 \pm 3$  days and an amplitude of 0.4 mmag in three out of five seasons of WASP data. We expect these signals in the HARPS data are due to magnetic activity and rotation of the star. We also see repeated signals in the in the various HARPS activity indicators including peak periods of  $\sim 28$  days in the Cross Correlation Function (CCF) Full-Width at Half-Maximum (FWHM),  $\sim 10$  days in the CCF Bisector Span (BIS), and  $\sim 30$  in the Mt Wilson ‘S index’

$S_{MW}$ , Na lines, and Ca lines. We show the GLS periodograms for the CCF FWHM, CCF BIS, and  $S_{MW}$  in Figure 2.

In order to account for this activity signal we applied a multi-dimensional Gaussian process (GP) approach, the `pyaneti` implementation of which is as described in Rajpaul et al. (2015). We use the quasi-periodic (QP) kernel, as defined by Roberts et al. (2013) and described in Barragán et al. (2022), and place an uninformative prior with a range of 5 to 45 days for the period of the QP kernel. We tested combinations of available activity indicators and in all cases the period of QP kernel was found to be at  $P_{GP} \sim 30$ -32 days, which we take to be the rotation period of the star. We found that a two-dimensional GP fit with the RV and BIS activity indicators gave the best results and obtained the lowest BIC value and smaller HARPS RV jitter value when we allow an RV jitter to be fit. With this fit we find a RV semi-amplitude of  $K = 4.61^{+1.79}_{-1.75} \text{ m s}^{-1}$  corresponding to a mass of  $M_p = 6.2^{+2.4}_{-2.3} M_{\oplus}$  for the 1-day planet and a  $P_{GP} = 31.22^{+0.99}_{-1.27}$  days. We show the multi-dimensional GP fit with BIS and the HARPS RV residuals in Figure 3.

For the previous fits we fixed the eccentricity of the 1-day period planet to 0. We also tested for eccentricity by fitting for  $e \cos \omega$  and  $e \sin \omega$ . The fit finds an eccentricity of  $e = 0.20^{+0.24}_{-0.14}$ . However, the BIC is actually smaller by 3 for the fit with the eccentricity. Given the large errors on the eccentricity, the smaller BIC of the fixed eccentricity, and the physical likelihood that the planet is tidally locked we fix the eccentricity to 0. Additionally given the complexity of the activity and small planet signal we conclude we do not have the precision to measure the eccentricity of the 1-day planet with our HARPS data.

Given the short period of the 1-day planet signal and longer rotation period of the star, we also tested fitting only HARPS RVs that had multiple observations taken on a given night and fit each night as its own offset in order to constrain the RV semi-amplitude of only the planet signal, similar to the analysis presented in Hatzes et al. (2011) to obtain the mass of CoRoT-7b (Léger et al. 2009; Queloz et al. 2009). After removing RVs during transits, we had 12 different nights of HARPS data with two observations per night. Allowing each night to have its own RV offset and then fitting for a single Keplerian we found an RV semi-amplitude of  $K = 5.03^{+1.40}_{-1.40} \text{ m s}^{-1}$  corresponding to a mass of  $M_p = 6.7^{+1.9}_{-1.9} M_{\oplus}$ , which is consistent with our Keplerian plus GP model of the residuals. However, the orbital phase coverage is not optimal which may explain the small differences with other analyses.

### 3.2.3. Three-planet RV-only Model

Finally for our RV-only analysis we perform a three-planet fit plus a linear trend and a QP GP kernel. We only use a 1-dimensional GP as `pyaneti` cannot fit activity indicators for one instrument and not others, and we do not find a good fit when including the CORALIE activity indicators which are essentially noise when trying to fit the activity signal. We put Gaussian priors on the periods and ephemerides of the two inner planets based on our transit fit in Section 3.3. For the outer planet period we used uniform priors between 1700 and 1900 days. We also put uniform priors on the QP GP period between 30 and 32 days based on our results from the 2-dimensional GP modeling with the HARPS residuals. We fixed the 1-day planet’s eccentricity to 0. All other parameters were given uniform priors. We show our full fit to the RV data in Figure 5 and present the fit parameters including our mass measurements in Table 2, which is in agreement with our previous analyses.

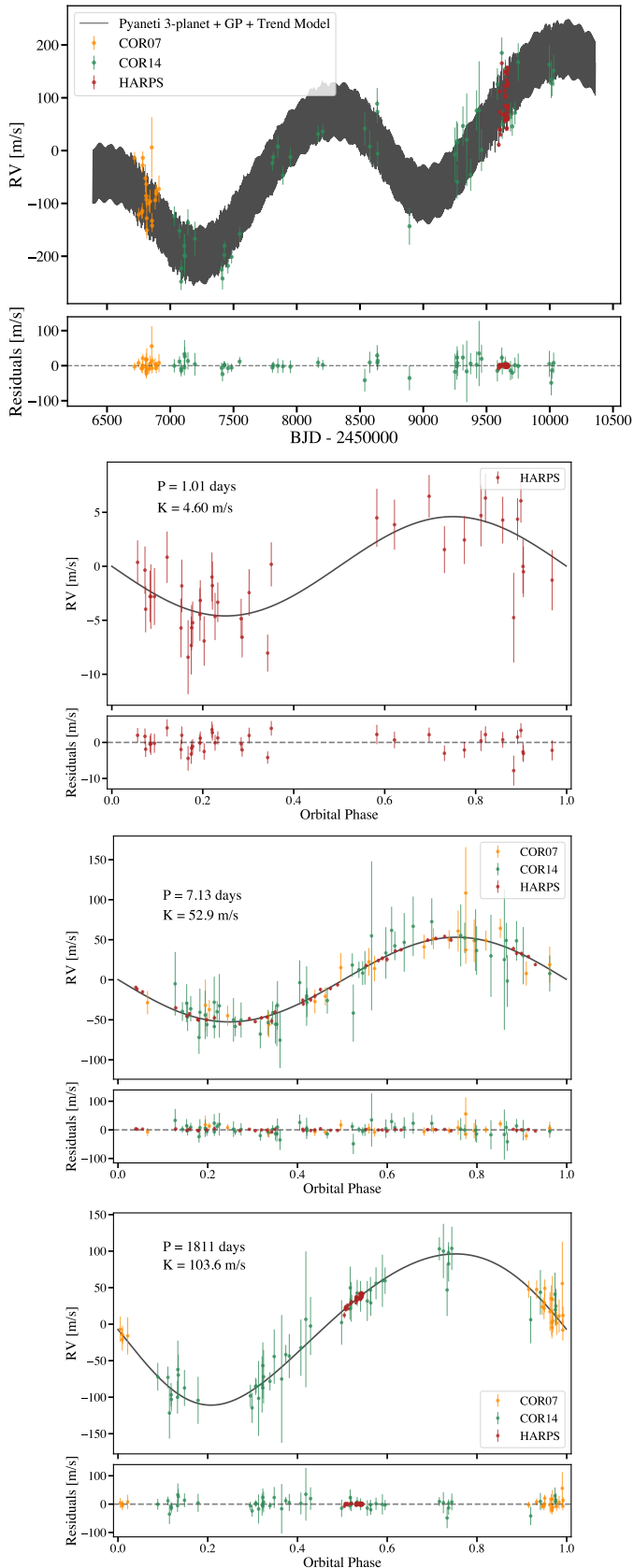


**Fig. 5.** *pyaneti* fit to RV data including three Keplerian models, a linear trend, and a GP described in Section 3.2.2. The lower three plots show the phased RV curves of the 1-day, 7-day, and ~1811-day outer planet respectively.

**Table 2.** *Pyaneti* initial RV fit parameters of WASP-132.

Parameter	Value
$T0_c$ [BJD_TDB]	$2458597.5761^{+0.0025}_{-0.0023}$
$P_c$ [days]	$1.0115337 \pm 0.0000050$
$ecc_c$	0 (fixed)
$\omega_c$ [deg]	$178^{+122}_{-122}$
$K_c$ [ $m s^{-1}$ ]	$4.60^{+1.37}_{-1.28}$
$M_c$ [ $M_{\oplus}$ ]	$6.20^{+1.84}_{-1.72}$
$T0_b$ [BJD_TDB]	$2459337.60557^{+0.00010}_{-0.00010}$
$P_b$ [days]	$7.1335139^{+0.000037}_{-0.000039}$
$ecc_b$	$0.0119^{+0.0110}_{-0.0082}$
$\omega_b$ [deg]	$66.7^{+246.7}_{-50.5}$
$K_b$ [ $m s^{-1}$ ]	$52.85^{+1.34}_{-1.28}$
$M_b$ [ $M_{Jup}$ ]	$0.427^{+0.018}_{-0.018}$
$T0_d$ [BJD_TDB]	$2455059.5^{+95.0}_{-88.3}$
$P_d$ [days]	$1811.8^{+42.6}_{-44.4}$
$ecc_d$	$0.100^{+0.078}_{-0.068}$
$\omega_d$ [deg]	$135.2^{+30.1}_{-37.1}$
$K_d$ [ $m s^{-1}$ ]	$103.6^{+9.6}_{-8.8}$
$M_d \sin i$ [ $M_{Jup}$ ]	$5.29^{+0.48}_{-0.46}$
COR07 RV [ $km s^{-1}$ ]	$31.1188^{+0.0252}_{-0.0328}$
COR14 RV [ $km s^{-1}$ ]	$31.1313^{+0.0053}_{-0.0057}$
HARPS RV [ $km s^{-1}$ ]	$31.1854^{+0.0093}_{-0.0097}$
jitter <sub>COR07</sub> [ $m s^{-1}$ ]	$1.95^{+4.29}_{-1.57}$
jitter <sub>COR14</sub> [ $m s^{-1}$ ]	$1.68^{+3.33}_{-1.33}$
jitter <sub>HARPS</sub> [ $m s^{-1}$ ]	$1.62^{+0.78}_{-0.90}$
linear trend [ $m s^{-1} d^{-1}$ ]	$0.0645^{+0.0066}_{-0.0070}$
GP A0 [ $km s^{-1}$ ]	$0.0077^{+0.0047}_{-0.0051}$
GP A1 [ $km s^{-1}$ ]	$0.052^{+0.043}_{-0.031}$
GP $\lambda_e$ [days]	$62.5^{+26.3}_{-33.9}$
GP $\lambda_p$ [days]	$0.59^{+0.27}_{-0.18}$
GP Period [days]	$31.42^{+0.37}_{-0.59}$

### 3.3. Joint Photometry and RV analysis

We modeled both the photometry and RV data with *juliet* (Espinoza et al. 2019), which uses Bayesian inference to model a set number of planetary signals using *batman* (Kreidberg 2015) to model the planetary transits and *radvel* (Fulton et al. 2018) to model the RVs. Of note, although *juliet* cannot handle multi-dimensional Gaussian processes (GPs) for RV data, for light curves *juliet* can model stellar activity as well as instrumental systematics with GPs (e.g., Gibson 2014) or simpler parametric functions, which we do not find available in *pyaneti*. For the transit model, *juliet* performs an efficient parameterization by fitting for the parameters  $r_1$  and  $r_2$  to ensure uniform exploration of the  $p$  (planet-to-star ratio;  $R_p/R_*$ ) and  $b$  (impact parameter) parameter space. We used the nested sampling method *dynesty* (Speagle 2019) implemented in *juliet* with 1500 live points and we ran the fit until the estimated uncertainty on the log-evidence was smaller than 0.1.

We added a white-noise jitter term in quadrature to the error bars of both the photometry and RV data to account for underestimated uncertainties and additional noise that was not captured by the model. To account for possible residual systematics and activity affecting the transit fit of TESS Sectors 11, 38, and 65, we fit a Gaussian process (GP) using a Matérn-3/2 kernel via *celerite* (Foreman-Mackey et al. 2017) within the *juliet* framework. In addition to the stellar activity fitting presented in

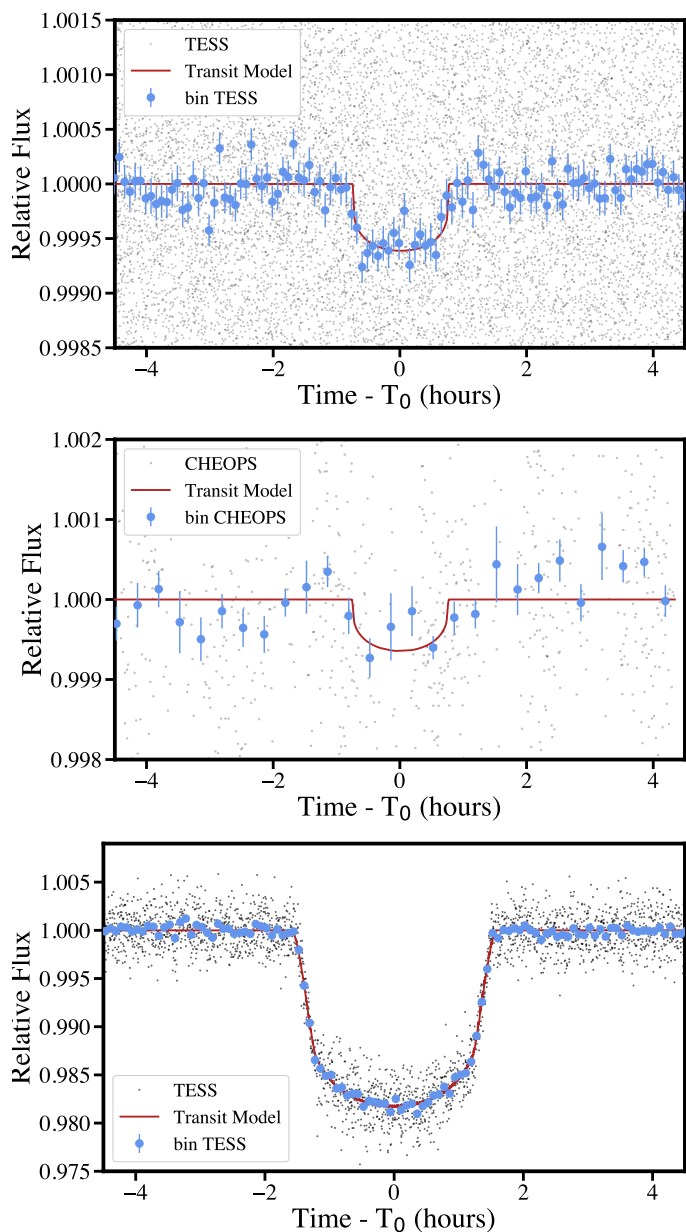


**Fig. 6.** Phased fit to WASP-132 c with all three TESS sectors. (*top*). Phased fit to WASP-132 c with CHEOPS. (*middle*). Phased fit to WASP-132 b with all three TESS sectors (*bottom*). The transit fit from *juliet* is described in Section 3.3. 5-minute TESS bins and 20-minute CHEOPS bins are shown for display purposes.

Section 3.2.2, a GP can account for correlated noise of various origins and propagates the uncertainty (e.g., Gibson et al. 2012; Gibson 2014). Additionally, properly fitting out of transit data will more accurately set the baseline for in transit data. We display the GP fit to the full TESS light curves in Figure A.1. We also fit a Gaussian process (GP) using a Matérn-3/2 kernel for the RV data and put uniform priors on the time-scale based on our initial RV analysis in Section 3.2.3. We fit the CHEOPS data by detrending with the background flux and the roll angle  $\phi$  by using  $\cos(\phi)$ ,  $\cos(2\phi)$ ,  $\sin(\phi)$ , and  $\sin(2\phi)$ . We display our full fit to the CHEOPS data in Figure A.2.

For limb darkening, we derived quadratic coefficients and their uncertainties for different photometric filters using the

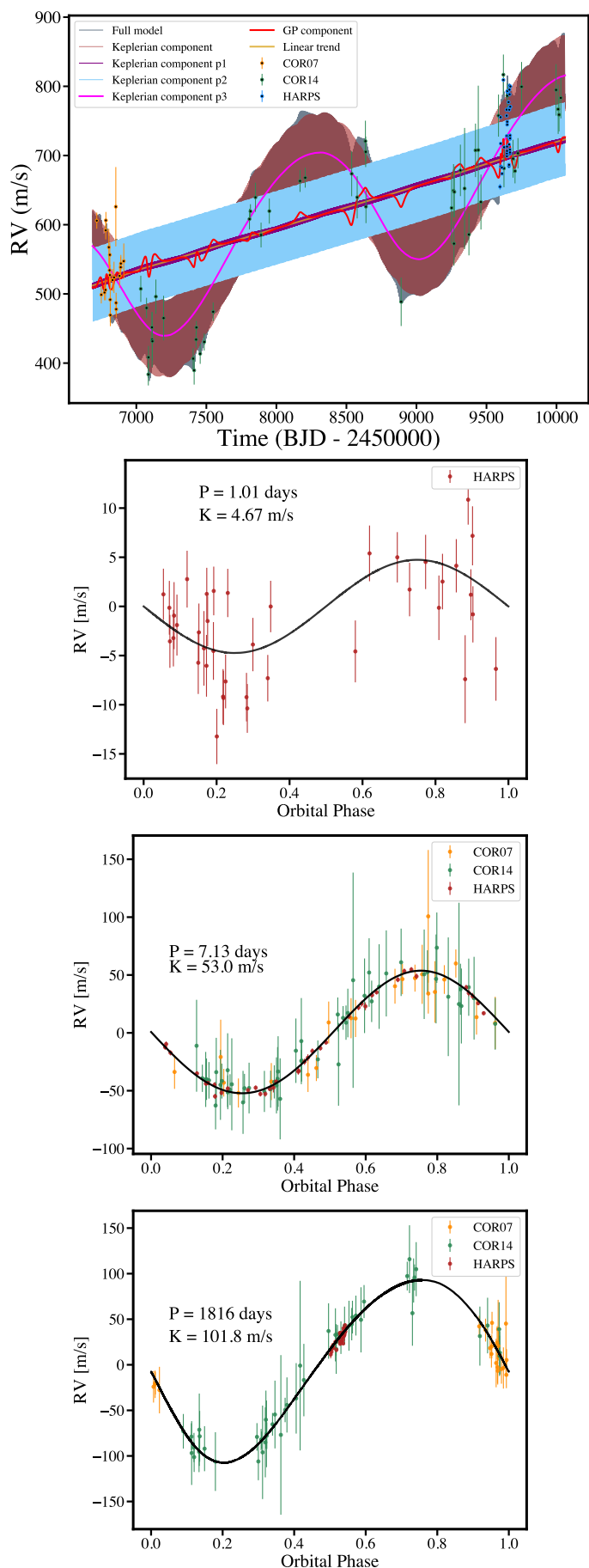


**Fig. 7.** RV fit from global *juliet* model to WASP-132. The top plot shows the full RV set with the different model components. The second from the top shows the phased RV data and *juliet* fit to planet c with only the HARPS data plotted, while the bottom two plots show planets b and d, respectively, with both HARPS and CORALIE data.

**Table 3.** WASP-132 planet parameters from `juliet`: Median and 68% confidence interval.

Parameter	Prior distribution*	Value
<b>Planet c</b>		
$P$ . . . . .	Period (days) . . . . .	$\mathcal{N}(1.0115, 0.001)$ . . . . .
$T_0$ . . . . .	Time of transit center (BJD <sub>TDB</sub> ) . . . . .	$\mathcal{N}(2458597.576, 0.001)$
$e$ . . . . .	Eccentricity of the orbit . . . . .	<i>fixed</i> . . . . .
$K$ . . . . .	Radial velocity semi-amplitude (m s <sup>-1</sup> ) . . . . .	$\mathcal{N}(4.60, 1.37)$ . . . . .
$\omega$ . . . . .	Argument of periastron (deg) . . . . .	$\mathcal{U}(0, 360)$ . . . . .
$r_1$ . . . . .	Parametrization for p and b . . . . .	$\mathcal{U}(0, 1)$ . . . . .
$r_2$ . . . . .	Parametrization for p and b . . . . .	$\mathcal{U}(0, 1)$ . . . . .
$i$ . . . . .	Inclination (deg) . . . . .	0
$p = R_p/R_\star$	Planet-to-star radius ratio . . . . .	0.405 <sup>+0.041</sup> <sub>-0.041</sub>
$b$ . . . . .	Impact parameter of the orbit . . . . .	0.02230 <sup>+0.00060</sup> <sub>-0.00065</sub>
$a$ . . . . .	Semi-major axis (AU) . . . . .	88.82 <sup>+0.67</sup> <sub>-0.69</sub>
$M_p$ . . . . .	Planetary mass ( $M_\oplus$ ) . . . . .	0.02230 <sup>+0.00060</sup> <sub>-0.00065</sub>
$R_p$ . . . . .	Planetary radius ( $R_\oplus$ ) . . . . .	0.107 <sup>+0.062</sup> <sub>-0.061</sub>
$\rho_p$ . . . . .	Planetary density (g cm <sup>-3</sup> ) . . . . .	0.01833 <sup>+0.00079</sup> <sub>-0.00079</sub>
$S$ . . . . .	Insolation ( $S_\oplus$ ) . . . . .	6.26 <sup>+1.84</sup> <sub>-1.83</sub>
$T_{eq}$ . . . . .	Equilibrium Temperature (K) . . . . .	1.841 <sup>+0.094</sup> <sub>-0.093</sub>
$T_{dur}$ . . . . .	Total Transit Duration (hours) . . . . .	5.47 <sup>+1.96</sup> <sub>-1.71</sub>
<b>Planet b</b>		
$P$ . . . . .	Period (days) . . . . .	$\mathcal{U}(7.1335 \pm 0.1)$ . . . . .
$T_0$ . . . . .	Time of transit center (BJD <sub>TDB</sub> ) . . . . .	$\mathcal{U}(2459337.6 \pm 0.2)$ . . . . .
$e$ . . . . .	Eccentricity of the orbit . . . . .	$\mathcal{B}(0.867, 3.03)$ . . . . .
$K$ . . . . .	Radial velocity semi-amplitude (m s <sup>-1</sup> ) . . . . .	$\mathcal{U}(0, 1000)$ . . . . .
$\omega$ . . . . .	Argument of periastron (deg) . . . . .	$\mathcal{U}(0, 360)$ . . . . .
$r_1$ . . . . .	Parametrization for p and b . . . . .	$\mathcal{U}(0, 1)$ . . . . .
$r_2$ . . . . .	Parametrization for p and b . . . . .	$\mathcal{U}(0, 1)$ . . . . .
$i$ . . . . .	Inclination (deg) . . . . .	7.1335164 <sup>+0.000019</sup> <sub>-0.000019</sub>
$p = R_p/R_\star$	Planet-to-star radius ratio . . . . .	2459337.60808 <sup>+0.00014</sup> <sub>-0.00016</sub>
$b$ . . . . .	Impact parameter of the orbit . . . . .	0.0163 <sup>+0.0067</sup> <sub>-0.0069</sub>
$a$ . . . . .	Semi-major axis (AU) . . . . .	52.99 <sup>+0.75</sup> <sub>-0.74</sub>
$M_p$ . . . . .	Planetary mass ( $M_{Jup}$ ) . . . . .	$\mathcal{U}(0, 1000)$ . . . . .
$R_p$ . . . . .	Planetary radius ( $R_{Jup}$ ) . . . . .	318 <sup>+31</sup> <sub>-298</sub>
$\rho_p$ . . . . .	Planetary density (g cm <sup>-3</sup> ) . . . . .	0.4535 <sup>+0.0250</sup> <sub>-0.0281</sub>
$S$ . . . . .	Insolation ( $S_\oplus$ ) . . . . .	0.12219 <sup>+0.00060</sup> <sub>-0.00052</sub>
$T_{eq}$ . . . . .	Equilibrium Temperature (K) . . . . .	89.46 <sup>+0.13</sup> <sub>-0.11</sub>
$T_{dur}$ . . . . .	Total Transit Duration (hours) . . . . .	0.12219 <sup>+0.00050</sup> <sub>-0.00052</sub>
<b>Planet d</b>		
$P$ . . . . .	Period (days) . . . . .	$\mathcal{N}(1812, 44)$ . . . . .
$T_0$ . . . . .	Time of transit center (BJD <sub>TDB</sub> ) . . . . .	$\mathcal{N}(2455059.5, 95)$ . . . . .
$e$ . . . . .	Eccentricity of the orbit . . . . .	$\mathcal{N}(0.1, 0.08)$ . . . . .
$K$ . . . . .	Radial velocity semi-amplitude (m s <sup>-1</sup> ) . . . . .	$\mathcal{N}(104, 9.6)$ . . . . .
$\omega$ . . . . .	Argument of periastron (deg) . . . . .	$\mathcal{N}(135, 40)$ . . . . .
$a$ . . . . .	Semi-major axis (AU) . . . . .	1816.6 <sup>+44.4</sup> <sub>-44.4</sub>
$M_p \sin i$ . . . . .	Planetary mass $\times$ sine inclination ( $M_{Jup}$ ) . . . . .	2455051.5 <sup>+95.0</sup> <sub>-95.0</sub>
$S$ . . . . .	Insolation ( $S_\oplus$ ) . . . . .	0.120 <sup>+0.078</sup> <sub>-0.078</sub>
$T_{eq}$ . . . . .	Equilibrium Temperature (K) . . . . .	101.81 <sup>+9.60</sup> <sub>-9.60</sub>
		131 <sup>+40</sup> <sub>-40</sub>
		2.71 <sup>+0.12</sup> <sub>-0.12</sub>
		5.16 <sup>+0.52</sup> <sub>-0.52</sub>
		0.0363 <sup>+0.0034</sup> <sub>-0.0030</sub>
		107 <sup>+11</sup> <sub>-18</sub>

\* $\mathcal{U}(a, b)$  indicates a uniform distribution between  $a$  and  $b$ ;  $\mathcal{J}(a, b)$  a Jeffrey or log-uniform distribution between  $a$  and  $b$ ;  $\mathcal{N}(a, b)$  a normal distribution with mean  $a$  and standard deviation  $b$ ; and  $\mathcal{B}(a, b)$  a Beta prior as detailed in Kipping (2014). Parameters with no prior distribution were derived. We sample from a normal distribution for the stellar mass, stellar radius, and stellar temperature, that are based on the results from Section 3.1 to derive parameters. †Uncertainties account for the priors set from the initial RV fit.

LDCU<sup>5</sup> routine (Deline et al. 2022) and used them to set Gaussian priors on the limb-darkening parameters. We used uniform priors for the period and transit center times. We fixed the eccentricity for the 1-day period planet and added a Beta prior for transiting planets for the hot Jupiter, as described in Kipping (2014). We used the  $\rho_*$  (stellar density) as a parameter instead of the scaled semi-major axis ( $a/R_\star$ ). The normal prior on stellar density is informed by the stellar analysis in Section 3.1.

For our final RV and photometry joint fit we constrained the RV semi-amplitude  $K$  of planet c as well as the period,  $T_0$ , ec-

centricity, RV  $K$ , and  $\omega$  of planet d using values from our initial `pyaneti` RV analysis presented in Section 3.2.2. We tested several times putting less constraints on these parameters within the `juliet` global model but found that the model would get stuck with solutions that had lower likelihoods than our final solution. We therefore used priors from our initial `pyaneti` analysis to guide the `juliet` global model to find the most likely solution. We account for these priors in our uncertainties of the modeled and derived `juliet` parameters.

Tables 3 and 4 display all of the modeled parameters as well as their input priors for our joint RV and transit model. Figure

<sup>5</sup> <https://github.com/delinea/LDCU>

**Table 4.** WASP-132 system and instrumental parameters from `juliet`: Median and 68% confidence interval.

Parameter		Prior distribution*	Value
$\rho_*$ . . . . .	Stellar density ( $\text{g cm}^{-3}$ ) . . . . .	$\mathcal{N}(2.56, 0.21)$ . . . . .	$2.602^{+0.067}_{-0.070}$
$q_{1,\text{TESS}}$ . . . . .	Quadratic limb-darkening parametrization . . . . .	$\mathcal{N}(0.428, 0.017)$ . . . . .	$0.4228^{+0.0155}_{-0.0152}$
$q_{2,\text{TESS}}$ . . . . .	Quadratic limb-darkening parametrization . . . . .	$\mathcal{N}(0.370, 0.025)$ . . . . .	$0.3597^{+0.0177}_{-0.0183}$
$q_{1,\text{CHEOPS}}$ . . . . .	Quadratic limb-darkening parametrization . . . . .	$\mathcal{N}(0.529, 0.019)$ . . . . .	$0.5245^{+0.0153}_{-0.0153}$
$q_{2,\text{CHEOPS}}$ . . . . .	Quadratic limb-darkening parametrization . . . . .	$\mathcal{N}(0.428, 0.022)$ . . . . .	$0.4272^{+0.0202}_{-0.0193}$
$m_{\text{flux,TESS11}}$ . . . . .	Offset (relative flux) . . . . .	$\mathcal{N}(0, 0.01)$ . . . . .	$-0.0076^{+0.0059}_{-0.0060}$
$m_{\text{flux,TESS38}}$ . . . . .	Offset (relative flux) . . . . .	$\mathcal{N}(0, 0.01)$ . . . . .	$0.0082^{+0.0073}_{-0.0069}$
$m_{\text{flux,TESS65}}$ . . . . .	Offset (relative flux) . . . . .	$\mathcal{N}(0, 0.01)$ . . . . .	$-0.0020^{+0.0064}_{-0.0064}$
$m_{\text{flux,CHEOPS}}$ . . . . .	Offset (relative flux) . . . . .	$\mathcal{N}(0, 0.01)$ . . . . .	$-0.00013^{+0.00012}_{-0.00012}$
$\sigma_{\text{TESS11}}$ . . . . .	Jitter (ppm) . . . . .	$\mathcal{J}(10^{-5}, 100.0)$ . . . . .	$0.086^{+5.820}_{-0.082}$
$\sigma_{\text{TESS38}}$ . . . . .	Jitter (ppm) . . . . .	$\mathcal{J}(10^{-5}, 100.0)$ . . . . .	$0.034^{+3.102}_{-0.033}$
$\sigma_{\text{TESS65}}$ . . . . .	Jitter (ppm) . . . . .	$\mathcal{J}(10^{-5}, 100.0)$ . . . . .	$0.106^{+6.306}_{-0.106}$
$\sigma_{\text{CHEOPS}}$ . . . . .	Jitter (ppm) . . . . .	$\mathcal{J}(10^{-5}, 100.0)$ . . . . .	$0.0029^{+0.1605}_{-0.0028}$
$\sigma_{\text{GP,TESS11}}$ . . . . .	GP amplitude (relative flux) . . . . .	$\mathcal{J}(10^{-6}, 1)$ . . . . .	$0.0155^{+0.0033}_{-0.0043}$
$\sigma_{\text{GP,TESS38}}$ . . . . .	GP amplitude (relative flux) . . . . .	$\mathcal{J}(10^{-6}, 1)$ . . . . .	$0.0240^{+0.0064}_{-0.0056}$
$\sigma_{\text{GP,TESS65}}$ . . . . .	GP amplitude (relative flux) . . . . .	$\mathcal{J}(10^{-6}, 1)$ . . . . .	$0.0895^{+0.0265}_{-0.0236}$
$\rho_{\text{GP,TESS11}}$ . . . . .	Photometry GP time-scale (days) . . . . .	$\mathcal{N}(31.3, 5.0)$ . . . . .	$30.16^{+3.96}_{-4.72}$
$\rho_{\text{GP,TESS38}}$ . . . . .	Photometry GP time-scale (days) . . . . .	$\mathcal{N}(31.3, 5.0)$ . . . . .	$30.41^{+4.12}_{-4.31}$
$\rho_{\text{GP,TESS65}}$ . . . . .	Photometry GP time-scale (days) . . . . .	$\mathcal{N}(31.3, 5.0)$ . . . . .	$29.21^{+4.03}_{-5.40}$
$\theta_{0\text{CHEOPS}}$ . . . . .	Detrending Parameter . . . . .	$\mathcal{U}(-0.1, 0.1)$ . . . . .	$0.000566^{+0.000084}_{-0.000077}$
$\theta_{1\text{CHEOPS}}$ . . . . .	Detrending Parameter . . . . .	$\mathcal{U}(-0.1, 0.1)$ . . . . .	$-0.000512^{+0.000069}_{-0.000068}$
$\theta_{2\text{CHEOPS}}$ . . . . .	Detrending Parameter . . . . .	$\mathcal{U}(-0.1, 0.1)$ . . . . .	$0.000936^{+0.000104}_{-0.000099}$
$\theta_{3\text{CHEOPS}}$ . . . . .	Detrending Parameter . . . . .	$\mathcal{U}(-0.1, 0.1)$ . . . . .	$0.000240^{+0.000046}_{-0.000046}$
$\theta_{4\text{CHEOPS}}$ . . . . .	Detrending Parameter . . . . .	$\mathcal{U}(-0.1, 0.1)$ . . . . .	$0.001940^{+0.000671}_{-0.000688}$
$\sigma_{\text{GP,RV}}$ . . . . .	RV GP amplitude ( $\text{m s}^{-1}$ ) . . . . .	$\mathcal{U}(0.01, 100)$ . . . . .	$42.48^{+6.43}_{-5.91}$
$\rho_{\text{GP,RV}}$ . . . . .	RV GP time-scale (days) . . . . .	$\mathcal{U}(29.3, 33.3)$ . . . . .	$30.03^{+0.81}_{-0.54}$
$\mu_{\text{COR07}}$ . . . . .	Systemic RV offset ( $\text{km s}^{-1}$ ) . . . . .	$\mathcal{U}(-100, 100)$ . . . . .	$30.505^{+0.333}_{-0.267}$
$\sigma_{\text{COR07}}$ . . . . .	Jitter ( $\text{m s}^{-1}$ ) . . . . .	$\mathcal{U}(0, 2)$ . . . . .	$0.968^{+0.580}_{-0.561}$
$\mu_{\text{COR14}}$ . . . . .	Systemic RV offset ( $\text{km s}^{-1}$ ) . . . . .	$\mathcal{U}(-100, 100)$ . . . . .	$30.512^{+0.326}_{-0.259}$
$\sigma_{\text{COR14}}$ . . . . .	Jitter ( $\text{m s}^{-1}$ ) . . . . .	$\mathcal{U}(0, 2)$ . . . . .	$0.94^{+0.59}_{-0.54}$
$\mu_{\text{HARPS}}$ . . . . .	Systemic RV offset ( $\text{km s}^{-1}$ ) . . . . .	$\mathcal{U}(-100, 100)$ . . . . .	$30.551^{+0.327}_{-0.257}$
$\sigma_{\text{HARPS}}$ . . . . .	Jitter ( $\text{m s}^{-1}$ ) . . . . .	$\mathcal{U}(0, 2)$ . . . . .	$1.63^{+0.257}_{-0.40}$
$A_{\text{RV}}$ . . . . .	slope of linear long-term RV trend ( $\text{m s}^{-1}\text{day}^{-1}$ ) . . . . .	$\mathcal{N}(0.0645, 0.01)$ . . . . .	$0.0648^{+0.0063}_{-0.0063}$
$B_{\text{RV}}$ . . . . .	intercept of linear long-term RV trend ( $\text{m s}^{-1}$ ) . . . . .	$\mathcal{U}(-1000, 1000)$ . . . . .	$611.9^{+260.6}_{-326.9}$

\*Prior symbols are the same as those described in Table 3.

6 displays the final model fits to the phased photometry data for both WASP-132 c and WASP-132 b. Figure 7 displays the final RV fits with the joint RV and photometry model. We find the planet masses to be consistent with our RV-only analysis and therefore present the joint fit as our final parameters.

In addition to all of the modeled parameters, Table 3 also displays derived planet parameters including the inclination, impact parameter, semi-major axis, and radius. We calculated the insolation using the equation:

$$S[S_{\oplus}] = L_*[L_{\odot}] (a[\text{AU}])^{-2}. \quad (1)$$

We calculated the equilibrium temperature assuming a Bond albedo of  $A = 0.343$  (the same as Jupiter's) for the hot Jupiter and  $A = 0.3$  (the same as Earth's) for the super-Earth and the semi-major axis distance  $a$  using the equation:

$$T_{\text{eq}} = T_{\text{eff}}(1 - A)^{1/4} \sqrt{\frac{R_*}{2a}}. \quad (2)$$

We set upper and lower uncertainties for the equilibrium temperature by assuming Bond albedos of  $A = 0$  and  $A = 0.686$  (double that of Jupiter), respectively for the hot and cold Jupiters and  $A = 0$  and  $A = 0.6$  (double that of Earth), respectively for the super-Earth.

## 4. Discussion

### 4.1. Comparison to previous studies

We find our stellar parameters in agreement with Hord et al. (2022) and other previous studies. Hord et al. (2022) found a radius of  $10.05 \pm 0.28 R_{\oplus}$  and mass of  $121.9 \pm 21.9 M_{\oplus}$  for WASP-132 b, while Hellier et al. (2017) found a mass of  $130.3 \pm 9.5 M_{\oplus}$ . Notably Hord et al. (2022) included a fit for WASP-132 c in their RV analysis to obtain the mass of WASP-132 b. With a measurement  $136.1 \pm 4.8 M_{\oplus}$ , we decrease by a factor of two the mass uncertainty for WASP-132 b, and we find a similar radius of  $10.10 \pm 0.43 R_{\oplus}$ . Hord et al. (2022) found a radius of  $1.85 \pm 0.10 R_{\oplus}$  for WASP-132 c, which is similar to our result of  $1.841 \pm 0.094 R_{\oplus}$ .

### 4.2. Dynamical history

With the help of previous studies such as Dawson & Johnson 2018, Wu et al. (2023) recently gave a unified framework for short-period gas giant dynamical sculpting where hot and warm Jupiters emerge as a natural outcome of postdisk dynamical sculpting of gas giants in compact multi-planet systems. They propose that after the initial starting point from the disk evolution, planet-planet interactions can excite the eccentricities of some giant planets and push them into smaller orbits. This eccentric migration continuum can be divided into three regimes

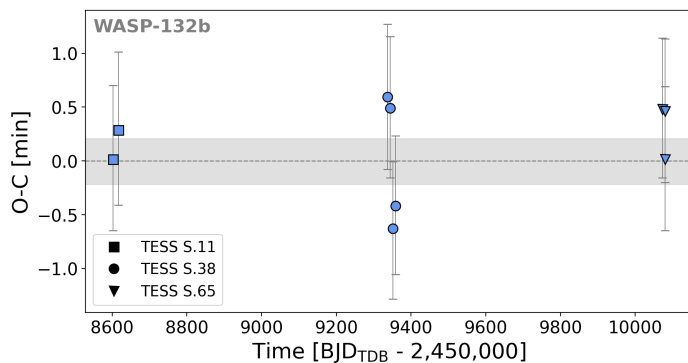


**Fig. 8.** TTVs of WASP-132 b determined with *juliet* on TESS data. The gray area represents the  $1\sigma$  uncertainty of the  $T_0$  from our global analysis.

of hot Jupiters, those with quiescent histories, low-eccentricity migration, and high-eccentricity migration (Wu et al. 2023). Given the presence of the small inner planet, WASP-132 b likely formed with a quiescent history without experiencing strong interactions with other planets in the system, maintaining low eccentricity (we find  $e \sim 0$  for WASP-132 b), and retaining nearby planetary companions. This scenario is more likely than low-eccentricity or high-eccentricity migration that involve interactions with other gas giants and are likely to remove nearby companions.

Although WASP-132 c and WASP-132 b are not in resonance, we performed a Transit Timing Variation (TTV) analysis of WASP-132 b to test if any other non-transiting or non-RV detected planets were causing perturbations of the planet. We conducted an analysis of the TTVs for WASP-132 b with *juliet* by utilizing all available photometric datasets from TESS. Instead of fitting a single period ( $P_{orb}$ ) and time-of-transit center ( $T_0$ ), *juliet* employed a method that seeks individual transit times. This approach involved fitting each transit independently and determining one transit time for each one, resulting in a more consistent and coherent analysis. Figure 8 illustrates the results of our analysis, which compares the observed transit times with the calculated linear ephemeris derived from all the transits. Notably, no significant variations were detected within the data.

Additionally, hot Jupiters in systems with two or more known stars could have been produced through eccentric migration triggered by secular Kozai-Lidov interactions with stellar companions (e.g., HD 80606 b; Naef et al. 2001; Wu & Murray 2003). Hord et al. (2022) presented speckle imaging of WASP-132 using the HRCam instrument on the 4.1 m SOAR telescope (Tokovinin 2018) and detected no nearby stars within  $3''$  of WASP-132. Hord et al. (2022) also observed WASP-132 with the LCOGT (Brown et al. 2013) 1.0 m network node at the South African Astronomical Observatory and ruled out nearby eclipsing binaries for all neighboring stars out to  $50''$  from WASP-132. However, in addition to the 2.7 AU outer planet, we also significantly detect a long-term trend in our CORALIE RVs. This could be due to an additional brown dwarf or low-mass star in the system. Using a basic calculation of mass from the RV span of  $\sim 200 \text{ m s}^{-1}$  (minimum  $K$ ), time span of  $\sim 9$  years (minimum period  $\sim 18$  years), and assuming a circular orbit, we find a potential minimum mass of this outer companion to be  $\sim 18.5 M_{Jup}$ . This possible additional brown dwarf or stellar companion could have influenced the migration of the two inner planets as well as the outer giant planet.

The stellar obliquity or the observed excess of spin-orbit misalignment can put important constraints on the formation pathways of hot Jupiters. If WASP-132 b did migrate early-on in the proto-planetary disk, measuring the spin-orbit angles of the two planets using the Rossiter-McLaughlin effect will allow the coplanarity of their orbits and their possible misalignments with the star to be assessed which constrains their dynamical history. As noted previously, ESPRESSO spectroscopic observations of the transits of both planets were obtained and are planned for publication by a separate team.

#### 4.3. Astrometric signal

Astrometry can be an ideal method to provide exact masses of companions in combination with RVs. A commonly applied approach analyses the proper motion anomaly between Hipparcos (ESA 1997) and Gaia (Gaia Collaboration et al. 2016b), described in more details by Snellen & Brown (2018) and Brandt et al. (2021). WASP-132 was too faint to be observed by Hipparcos, which means that the comparison is not possible; however, DR3 (Gaia Collaboration et al. 2023) includes an additional 12 months of observations more than DR2 (Gaia Collaboration et al. 2018b) and can be compared. The short-period planets are averaged into the proper motions reported by these two datasets, but the proper motion anomaly of WASP-132 d (1817 days) should be visible, if significant. Whereas the long term trend we detected in the RVs should be seen as a constant proper motion offset and will likely not introduce any difference between DR2 and DR3.

There is indeed a substantial difference ( $\Delta \mu_{\alpha^*} = -0.30 \text{ mas yr}^{-1}$ ) between the proper motion values in Right Ascension from DR3 ( $\mu_{\alpha^*} = 12.26 \pm 0.02 \text{ mas yr}^{-1}$ ) and DR2 ( $\mu_{\alpha^*} = 12.56 \pm 0.07 \text{ mas yr}^{-1}$ ). While the difference in proper motions in Declination ( $\Delta \mu_{\delta} = 0.04 \text{ mas yr}^{-1}$ ) is of the same order as the error margins (DR3  $\mu_{\delta} = -73.17 \pm 0.02 \text{ mas yr}^{-1}$  and DR2  $\mu_{\delta} = -73.21 \pm 0.07 \text{ mas yr}^{-1}$ ). As the proper motion of DR3 also includes the data of DR2, the difference in proper motion is an indication of astrometric signal. However, drawing conclusions about the exact mass requires extensive modeling beyond the scope of this paper.

Additionally, Gaia DR3 reports a Renormalized Unit Weight Error (RUWE) of 1.23, where 1 is generally seen as a good measurement and above 1.4 as binarity. A RUWE above 1.2, however, can already indicate a proper motion anomaly. In other words, Gaia detects the astrometric signal of a companion but does not necessarily confirm it as a binary system. The excess noise level, at 0.11, while relatively low, ideally should be zero, indicating modeling errors in either the excess noise associated with the source or the attitude noise. This excess noise is reported with a high significance (20.9). In conclusion, given the companion's minimal mass of  $5.16 M_{Jup}$  and the presence of a significant astrometric signal, it is plausible that WASP-132 d may be a brown dwarf.

#### 4.4. Internal characterization of the two giant planets

The available measurements of the mass and the radius of the planet WASP-132 b make it possible to infer its bulk heavy-element content with giant planet evolution models (e.g., Miller & Fortney 2011; Thorngren et al. 2016; Müller & Helled 2023a). This is an important piece of information since it can be compared to predictions from formation models and therefore be used as an additional constraint (e.g., Guillot et al. 2006; Jo-

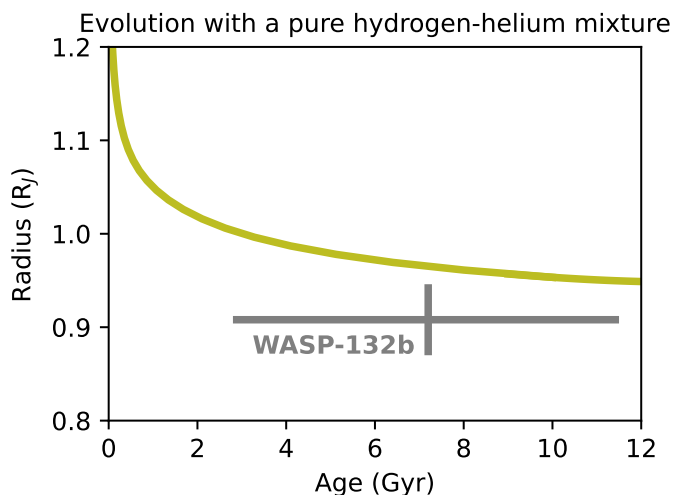


**Fig. 9.** The cooling of WASP-132 b assuming it has a pure hydrogen-helium composition (purple), with the grey error bars showing the measured values. It is clear that the planet must be enriched in heavy elements in order to match the observations.

hansen & Lambrechts 2017; Hasegawa et al. 2018). With a  $T_{eq} = 682$  K, WASP-132 b is significantly cooler than strongly irradiated hot Jupiters. This makes the inferred composition less uncertain since the planet should not be inflated (e.g., Fortney et al. 2021). Here, we used the giant planet evolution models from Müller & Helled (2021) to calculate the cooling of the planet. Fig. 9 shows the radius as a function of time assuming that the planet has zero metallicity. Comparing it to the observed radius, it is clear that the planet is not inflated compared to predictions from the model, and that it must be enriched with heavy elements.

To quantify the enrichment, we inferred the planet’s bulk heavy-element mass fraction  $Z$  in a Monte-Carlo fashion (see e.g., Müller & Helled 2023b, for a review): we create sample planets by drawing from the observed planetary mass, radius, and age distributions. For each sample, we calculate the evolution for a range of bulk metallicities in order to find which value would match the sampled radius at the right age. By repeating this process, the posterior distribution of the planet’s heavy-element mass can be estimated. The result is shown in Fig. 10. The posterior is roughly Gaussian, with a mean of  $\mu_Z = 13\%$  and a standard deviation of  $\sigma_Z = 6\%$ . This yields a heavy-element mass of  $M_Z \approx 17 M_{\oplus}$ , which is similar in magnitude to what would be expected from the critical core mass in core-accretion models (e.g., Helled et al. 2014). For comparison, if the planet had stellar metallicity, its heavy-element mass would be  $M_Z \approx 2.6 M_{\oplus}$ .

Since WASP-132 d does not have a measured radius, it is not possible to infer its bulk composition in the same way. However, we can provide a range of plausible radii by calculating its evolution from the measured  $M_p \sin i = 5.16 M_J$  for a range of bulk metallicities. We limited the models to  $0 < Z < 0.2$  since the upper bound would mean that the planet has about  $M_Z \approx 1 M_J$ , which would be very metal-rich. While such extreme enrichments exist, they are not very common (Thorngren et al. 2016). The cooling tracks are shown in Fig. 11.

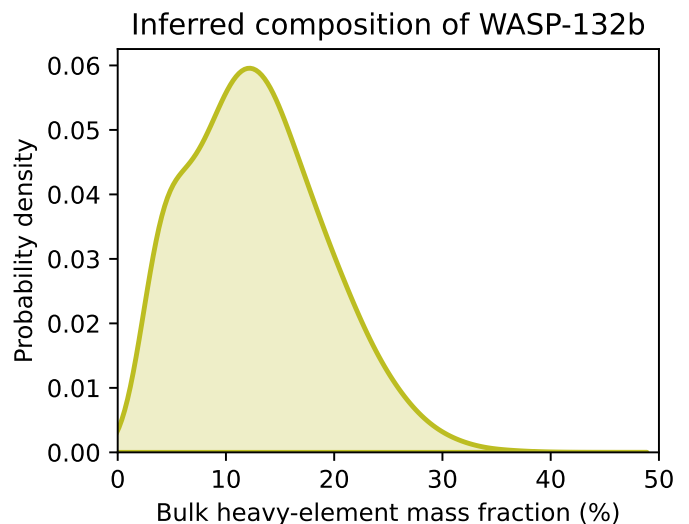


**Fig. 10.** Posterior distribution of the inferred heavy-element mass fraction of WASP-132b. The distribution is approximately Gaussian, with a mean of  $\mu_Z = 13\%$  and a standard deviation of  $\sigma_Z = 6\%$

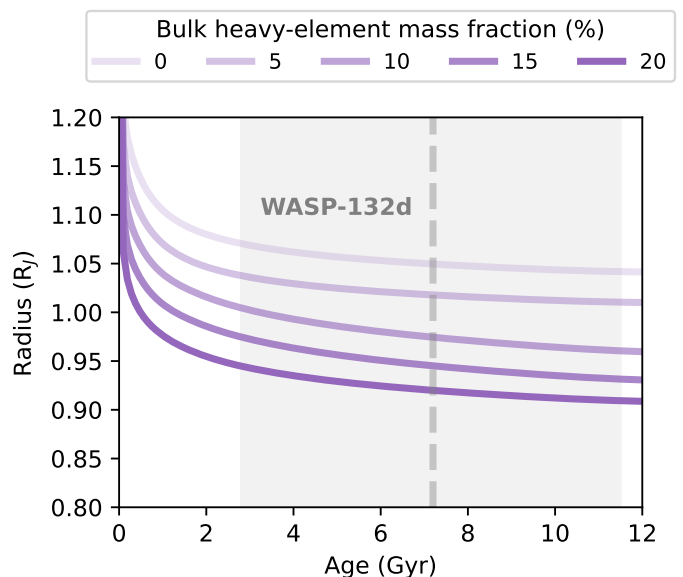


**Fig. 11.** The cooling of WASP-132d assuming bulk heavy-element fractions of  $Z = 0, 5, 10, 15$  and  $20\%$  (purple lines). The shaded grey area shows the stellar age and its uncertainties, with the dashed grey vertical line indicating the mean stellar age.

#### 4.5. Internal characterization of WASP-132 c

Figure 12 clearly shows that WASP-132 b sits slightly above the Earth-like composition line, suggesting a refractory-rich composition. To probe the scope of interior structures that are consistent with the observed constraints, we use the four layer model of Dorn et al. (2017). It includes an iron core, a rocky mantle, a water layer, and a hydrogen-helium atmosphere. Using a nested sampling algorithm (Buchner et al. 2014), we vary the layer masses, the elemental ratios of Mg/Si and Fe/Si in the mantle and the age of the planet, taking the stellar values for the priors. In order to put upper bounds on the water and atmospheric mass fractions we ran a model assuming no atmosphere (*no-atmosphere model*) and a model assuming no water layer (*no-water model*),

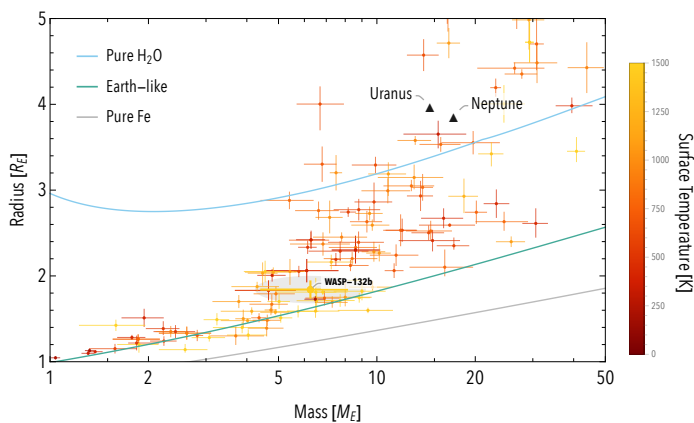


**Fig. 12.** Mass-radius diagram for WASP-132c. The lines show the mass-radius relation for a pure water model (blue), an Earth-like model (green), and a pure-iron model (gray). The other exoplanets are taken from the PlanetS catalogue (Otegi et al. 2020).

**Table 5.** WASP-132 c interior structure nested sampling results

Model	$M_{\text{core}}/M_p$	$M_{\text{mantle}}/M_p$	$M_{\text{water}}/M_p$	$\log(M_{\text{atm}}/M_p)$
<i>free</i>	$0.53 \pm 0.23$	$0.38 \pm 0.24$	$0.09 \pm 0.06$	$-8.54 \pm 1.85$
<i>no-atmosphere</i>	$0.50 \pm 0.23$	$0.38 \pm 0.24$	$0.11 \pm 0.06$	N/A
<i>no-water</i>	$0.47 \pm 0.26$	$0.53 \pm 0.26$	0.00	$-5.08 \pm 1.17$

respectively. Additionally, we ran a model where we put no constraints on the layer masses (*free model*). Our results are listed in Table 5.

All nested sampling models favor a refractory-rich composition which is dominated by metals and silicates and a negligible atmosphere. It should be noted, however, that the assumed internal structure is very simple. In reality, the internal structure of planets can be more complex, including enrichment of the atmosphere with heavy elements and the hydration of the mantle and/or core. Accounting for more sophisticated structure could affect the inferred results. However, our main conclusions that WASP-132c is an exoplanet dominated by refractory material are unlikely to change.

#### 4.6. WASP-132: a rare multi-planet system

Figure 13 shows a Mass-Radius diagram highlighting multi-planetary systems with precise densities ( $\sigma_M/M \leq 25\%$  and  $\sigma_R/R \leq 8\%$ ) from the PlanetS catalog (Otegi et al. 2020), and in particular systems composed of a hot or warm Jupiter ( $P < 100$  days) and a nearby small planet ( $R < 4 R_{\oplus}$ ). Among the 127 planets in 80 systems, only 6 have this particular configuration: WASP-132, WASP-47 (Bryant & Bayliss 2022), 55 Cnc (Bourrier et al. 2018), KOI-94 (Weiss et al. 2013), WASP-84 (Maciejewski et al. 2023) and KOI-142 (Weiss et al. 2020). This once again demonstrates the rare contribution of this system, and the mass measurement of WASP-132 c, to a very small existing population.

The small planets with accompanying hot Jupiters consist of five super-Earths and two sub-Neptunes. Considering the sub-Neptunes, WASP-47 d is located at a longer period than its hot Jupiter companion, while the super-Earth WASP-47 e is inside the hot Jupiter. KOI-142 b orbits with a much longer period than the other planets in this diagram ( $P = 10.92$  days), explaining its larger size due to lower irradiation. Its associated Jupiter is also less "hot".

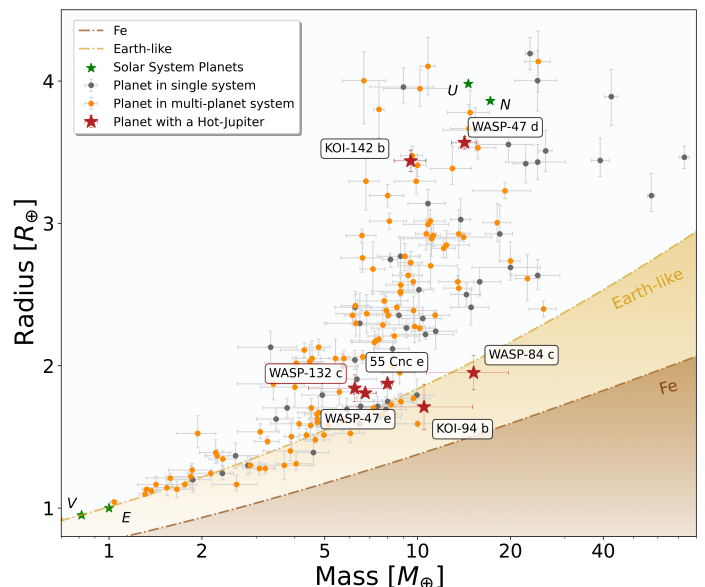


**Fig. 13.** Mass-radius diagram of small exoplanets with precise densities ( $\sigma_M/M \leq 25\%$  and  $\sigma_R/R \leq 8\%$ ) from the PlanetS catalog (Otegi et al. 2020). The red stars correspond to known small planets ( $R < 4 R_{\oplus}$ ), with precise radius and mass measurements, that have a hot or warm Jupiter companion ( $R > 0.8 R_{\text{Jup}}$ ). Orange dots are planets in multi-planet system of all kinds. Grey dots are planets in single-planet system. Composition lines are displayed for pure-iron (brown) and Earth-like planets (light-brown).

The super-Earths with hot or warm Jupiters are on the more massive end of this planet type and are likely composed of refractory elements. This may reveal that we are biased to detect the heaviest super-Earths in the presence of a hot Jupiter and lighter inner rocky planets in this kind of system may exist. Smaller planets like Kepler-730 c ( $R = 1.57 \pm 0.13 R_{\oplus}$ ; Cañas et al. 2019), which have no mass measurement, could be lighter. The lack of a similar system between the sub-Neptunes and super-Earths with hot Jupiters could be intimately linked to their short orbital period and therefore to the irradiation received, stripping these planets of their atmosphere. Hot Jupiters then play an important role behind, limiting an internal planet's period.

## 5. Conclusion

We report refined bulk measurements of the WASP-132 system. The 7.1-day hot Jupiter WASP-132 b was first discovered by WASP (Hellier et al. 2017) and an inner 1.01-day super-Earth was subsequently discovered by TESS (Hord et al. 2022). Here we also report the discovery of an 2.7 AU outer giant planet and long-term linear trend in the RVs suggestive of another outer companion. Using over nine years of CORALIE observations and highly-sampled HARPS data we determine the masses of the planets from smallest to largest orbital period to be  $M_p = 6.26^{+1.84}_{-1.83} M_{\oplus}$ ,  $M_p = 0.428^{+0.015}_{-0.015} M_{\text{Jup}}$ , and  $M_p \sin i = 5.16^{+0.52}_{-0.52} M_{\text{Jup}}$ , respectively. Using TESS and CHEOPS photometry data we measure the radii of the two inner transiting planets to be  $1.841^{+0.094}_{-0.093} R_{\oplus}$  and  $0.901^{+0.038}_{-0.038} R_{\text{Jup}}$ . We also performed an independent stellar analysis to find  $M_{\star} = 0.789 \pm 0.039 M_{\odot}$  and  $R_{\star} = 0.758 \pm 0.032 R_{\odot}$ . We find that the hot Jupiter WASP-132 b is not inflated and is enriched with heavy elements. For the super-Earth WASP-132 c, our internal structure modeling favors a refractory-rich composition that is

dominated by metals and silicates and a negligible atmosphere. We find that both the inner 1-day super-Earth and hot Jupiter are likely in circular orbits with eccentricities of  $\sim 0$ . Given the presence of a nearby inner-planet and its low-eccentricity, the hot Jupiter WASP-132 b likely migrated through quieter mechanisms than high-eccentricity migration making it a rare contribution to the current planet population.

**Acknowledgements.** We thank the Swiss National Science Foundation (SNSF) and the Geneva University for their continuous support to our planet low-mass companion search programs. This work was carried out in the frame of the Swiss National Centre for Competence in Research (NCCR) *PlanetS* supported by the SNSF including grants 51NF40\_182901 and 51NF40\_205606. This work used computations that were performed at the University of Geneva on the "Yggdrasil" High Performance Computing (HPC) clusters. This publication makes use of The Data & Analysis Center for Exoplanets (DACE), which is a facility based at the University of Geneva (CH) dedicated to extrasolar planet data visualization, exchange, and analysis. DACE is a platform of NCCR *PlanetS* and is available at <https://dace.unige.ch>. This paper includes data collected by the TESS mission. Funding for the TESS mission is provided by the NASA Explorer Program. We acknowledge the use of public TESS data from pipelines at the TESS Science Office and at the TESS Science Processing Operations Center. Resources supporting this work were provided by the NASA High-End Computing (HEC) Program through the NASA Advanced Supercomputing (NAS) Division at Ames Research Center for the production of the SPOC data products. V.A. acknowledges the support by FCT - Fundação para a Ciência e a Tecnologia through national funds (grants: UIDB/04434/2020, UIDP/04434/2020, and 2022.06962.PTDC). DJA is supported by UKRI through the STFC (ST/R00384X/1) and EPSRC (EP/X027562/1). NCS acknowledges the funding by the European Union (ERC, FIERCE, 101052347). Views and opinions expressed are however those of the author(s) only and do not necessarily reflect those of the European Union or the European Research Council. Neither the European Union nor the granting authority can be held responsible for them. This work was supported by FCT - Fundação para a Ciência e a Tecnologia through national funds and by FEDER through COMPETE2020 - Programa Operacional Competitividade e Internacionalização by these grants: UIDB/04434/2020; UIDP/04434/2020.

## References

- 1997, ESA Special Publication, Vol. 1200, The HIPPARCOS and TYCHO catalogues. Astrometric and photometric star catalogues derived from the ESA HIPPARCOS Space Astrometry Mission
- Adibekyan, V., Figueira, P., Santos, N. C., et al. 2015, *A&A*, 583, A94
- Adibekyan, V. Z., Sousa, S. G., Santos, N. C., et al. 2012, *A&A*, 545, A32
- Astropy Collaboration, Price-Whelan, A. M., Sipőcz, B. M., et al. 2018, *AJ*, 156, 123
- Astropy Collaboration, Robitaille, T. P., Tollerud, E. J., et al. 2013, *A&A*, 558, A33
- Bailer-Jones, C. A. L., Rybizki, J., Fouesneau, M., Mantelet, G., & Andrae, R. 2018, *AJ*, 156, 58
- Baluev, R. V. 2008, *MNRAS*, 385, 1279
- Barbato, D., Sozzetti, A., Desidera, S., et al. 2018, *A&A*, 615, A175
- Barragán, O., Aigrain, S., Rajpaul, V. M., & Zicher, N. 2022, *MNRAS*, 509, 866
- Barragán, O., Gandolfi, D., & Antoniciello, G. 2019, *MNRAS*, 482, 1017
- Baruteau, C., Crida, A., Paardekooper, S. J., et al. 2014, in *Protostars and Planets VI*, ed. H. Beuther, R. S. Klessen, C. P. Dullemond, & T. Henning, 667
- Becker, J. C., Vanderburg, A., Adams, F. C., Rappaport, S. A., & Schwengel, H. M. 2015, *ApJ*, 812, L18
- Benz, W., Broeg, C., Fortier, A., et al. 2021, *Experimental Astronomy*, 51, 109
- Berger, T. A., Huber, D., van Saders, J. L., et al. 2020, *AJ*, 159, 280
- Boisse, I., Bouchy, F., Hébrard, G., et al. 2011, *A&A*, 528, A4
- Bonfanti, A., Delrez, L., Hooton, M. J., et al. 2021, *A&A*, 646, A157
- Bonomo, A. S., Dumusque, X., Massa, A., et al. 2023, *A&A*, 677, A33
- Borucki, W. J., Koch, D., Basri, G., et al. 2010, *Science*, 327, 977
- Bourque, M., Espinoza, N., Filippazzo, J., et al. 2021, *The Exoplanet Characterization Toolkit (ExoCTK)*, Zenodo
- Bourrier, V., Dumusque, X., Dorn, C., et al. 2018, *A&A*, 619, A1
- Bovy, J., Rix, H.-W., Green, G. M., Schlafly, E. F., & Finkbeiner, D. P. 2016, *ApJ*, 818, 130
- Brandt, T. D., Dupuy, T. J., Li, Y., et al. 2021, *AJ*, 162, 186
- Broeg, C., Fortier, A., Ehrenreich, D., et al. 2013, in *European Physical Journal Web of Conferences*, Vol. 47, European Physical Journal Web of Conferences, 03005
- Brown, T. M., Baliber, N., Bianco, F. B., et al. 2013, *PASP*, 125, 1031
- Bryan, M. L., Knutson, H. A., Lee, E. J., et al. 2019, *AJ*, 157, 52
- Bryant, E. M. & Bayliss, D. 2022, *AJ*, 163, 197
- Buchner, J., Georgakakis, A., Nandra, K., et al. 2014, *A&A*, 564, A125
- Cañas, C. I., Wang, S., Mahadevan, S., et al. 2019, *ApJ*, 870, L17
- Cersullo, F., Wildi, F., Chazelas, B., & Pepe, F. 2017, *A&A*, 601, A102
- Chazelas, B., Pepe, F., & Wildi, F. 2012, in *Society of Photo-Optical Instrumentation Engineers (SPIE) Conference Series*, Vol. 8450, *Modern Technologies in Space- and Ground-based Telescopes and Instrumentation II*, ed. R. Navarro, C. R. Cunningham, & E. Prieto, 845013
- Choi, J., Dotter, A., Conroy, C., et al. 2016, *ApJ*, 823, 102
- Costa Silva, A. R., Delgado Mena, E., & Tsantaki, M. 2020, *A&A*, 634, A136
- Dawson, R. I. & Johnson, J. A. 2018, *ARA&A*, 56, 175
- Deline, A., Hooton, M. J., Lendl, M., et al. 2022, *A&A*, 659, A74
- Dorn, C., Venturini, J., Khan, A., et al. 2017, *A&A*, 597, A37
- Dotter, A. 2016, *ApJS*, 222, 8
- Doyle, A. P., Davies, G. R., Smalley, B., Chaplin, W. J., & Elsworth, Y. 2014, *MNRAS*, 444, 3592
- Eastman, J. D., Rodriguez, J. E., Agol, E., et al. 2019, arXiv e-prints, arXiv:1907.09480
- Espinoza, N., Kossakowski, D., & Brahm, R. 2019, *MNRAS*, 490, 2262
- Foreman-Mackey, D., Agol, E., Ambikasaran, S., & Angus, R. 2017, *AJ*, 154, 220
- Fortney, J. J., Dawson, R. I., & Komacek, T. D. 2021, *Journal of Geophysical Research (Planets)*, 126, e06629
- Fulton, B. J., Petigura, E. A., Blunt, S., & Sinukoff, E. 2018, *PASP*, 130, 044504
- Gaia Collaboration, Brown, A. G. A., Vallenari, A., et al. 2018a, *A&A*, 616, A1
- Gaia Collaboration, Brown, A. G. A., Vallenari, A., et al. 2018b, *A&A*, 616, A1
- Gaia Collaboration, Brown, A. G. A., Vallenari, A., et al. 2021, *A&A*, 649, A1
- Gaia Collaboration, Prusti, T., de Bruijne, J. H. J., et al. 2016a, *A&A*, 595, A1
- Gaia Collaboration, Prusti, T., de Bruijne, J. H. J., et al. 2016b, *A&A*, 595, A1
- Gaia Collaboration, Vallenari, A., Brown, A. G. A., et al. 2023, *A&A*, 674, A1
- Giacalone, S. & Dressing, C. D. 2020, *triceratops: Candidate exoplanet rating tool*, Astrophysics Source Code Library, record ascl:2002.004
- Giacalone, S., Dressing, C. D., Jensen, E. L. N., et al. 2021, *AJ*, 161, 24
- Gibson, N. P. 2014, *MNRAS*, 445, 3401
- Gibson, N. P., Aigrain, S., Roberts, S., et al. 2012, *MNRAS*, 419, 2683
- Goldreich, P. & Tremaine, S. 1980, *ApJ*, 241, 425
- Gomes da Silva, J., Santos, N. C., Adibekyan, V., et al. 2021, *A&A*, 646, A77
- Guillot, T., Santos, N. C., Pont, F., et al. 2006, *A&A*, 453, L21
- Hasegawa, Y., Bryden, G., Ikoma, M., Vasisht, G., & Swain, M. 2018, *ApJ*, 865, 32
- Hatzes, A. P., Fridlund, M., Nachmani, G., et al. 2011, *ApJ*, 743, 75
- Hébrard, G., Díaz, R. F., Correia, A. C. M., et al. 2020, *A&A*, 640, A32
- Helled, R., Bodenheimer, P., Podolak, M., et al. 2014, in *Protostars and Planets VI*, ed. H. Beuther, R. S. Klessen, C. P. Dullemond, & T. Henning, 643–665
- Hellier, C., Anderson, D. R., Collier Cameron, A., et al. 2017, *MNRAS*, 465, 3693
- Henden, A. A., Templeton, M., Terrell, D., et al. 2016, *VizieR Online Data Catalog*, II/336
- Henry, T. J., Soderblom, D. R., Donahue, R. A., & Baliunas, S. L. 1996, *AJ*, 111, 439
- Herman, M. K., Zhu, W., & Wu, Y. 2019, *AJ*, 157, 248
- Hippke, M. & Heller, R. 2019, *A&A*, 623, A39
- Hord, B. J., Colón, K. D., Berger, T. A., et al. 2022, *AJ*, 164, 13
- Hord, B. J., Colón, K. D., Kostov, V., et al. 2021, *AJ*, 162, 263
- Hoyer, S., Guterman, P., Demangeon, O., et al. 2020, *A&A*, 635, A24
- Huang, C., Wu, Y., & Triaud, A. H. M. J. 2016, *ApJ*, 825, 98
- Huang, C. X., Quinn, S. N., Vanderburg, A., et al. 2020, *ApJ*, 892, L7
- Huber, D., Zinn, J., Bojsen-Hansen, M., et al. 2017, *ApJ*, 844, 102
- Ivshina, E. S. & Winn, J. N. 2022, *ApJS*, 259, 62
- Izidoro, A., Raymond, S. N., Morbidelli, A., Hersant, F., & Pierens, A. 2015, *ApJ*, 800, L22
- Jehin, E., Gillon, M., Queloz, D., et al. 2011, *The Messenger*, 145, 2
- Jenkins, J. M. 2002, *ApJ*, 575, 493
- Jenkins, J. M., Chandrasekaran, H., McCauliff, S. D., et al. 2010, in *Society of Photo-Optical Instrumentation Engineers (SPIE) Conference Series*, Vol. 7740, *Software and Cyberinfrastructure for Astronomy*, ed. N. M. Radziwill & A. Bridger, 77400D
- Jenkins, J. M., Twicken, J. D., McCauliff, S., et al. 2016, in *Society of Photo-Optical Instrumentation Engineers (SPIE) Conference Series*, Vol. 9913, *Software and Cyberinfrastructure for Astronomy IV*, ed. G. Chiozzi & J. C. Guzman, 99133E
- Johansen, A. & Lambrechts, M. 2017, *Annual Review of Earth and Planetary Sciences*, 45, 359
- Kipping, D. M. 2014, *MNRAS*, 444, 2263
- Kreidberg, L. 2015, *PASP*, 127, 1161
- Kurucz, R. L. 1993, *SYNTHES spectrum synthesis programs and line data*
- Lambrechts, M., Morbidelli, A., Jacobson, S. A., et al. 2019, *A&A*, 627, A83
- Léger, A., Rouan, D., Schneider, J., et al. 2009, *A&A*, 506, 287
- Lin, D. N. C. & Ida, S. 1997, *ApJ*, 477, 781
- Lindgren, L., Bastian, U., Biermann, M., et al. 2021, *A&A*, 649, A4

- Lomb, N. R. 1976, *Ap&SS*, 39, 447
- Maciejewski, G., Golonka, J., Łoboda, W., et al. 2023, *MNRAS*, 525, L43
- Mamajek, E. E. & Hillenbrand, L. A. 2008, *ApJ*, 687, 1264
- Mayor, M., Pepe, F., Queloz, D., et al. 2003, *The Messenger*, 114, 20
- McLaughlin, D. B. 1924, *ApJ*, 60, 22
- Miller, N. & Fortney, J. J. 2011, *ApJ*, 736, L29
- Morton, T. D. 2012, *ApJ*, 761, 6
- Morton, T. D. 2015, VESPA: False positive probabilities calculator, *Astrophysics Source Code Library*, record ascl:1503.011
- Müller, S. & Helled, R. 2021, *MNRAS*, 507, 2094
- Müller, S. & Helled, R. 2023a, *A&A*, 669, A24
- Müller, S. & Helled, R. 2023b, *Frontiers in Astronomy and Space Sciences*, 10, 1179000
- Mustill, A. J., Davies, M. B., & Johansen, A. 2015, *ApJ*, 808, 14
- Naef, D., Latham, D. W., Mayor, M., et al. 2001, *A&A*, 375, L27
- Noyes, R. W., Hartmann, L. W., Baliunas, S. L., Duncan, D. K., & Vaughan, A. H. 1984, *ApJ*, 279, 763
- Otegi, J. F., Bouchy, F., & Helled, R. 2020, *A&A*, 634, A43
- Pecaut, M. J. & Mamajek, E. E. 2013, *ApJS*, 208, 9
- Pepe, F., Cristiani, S., Rebolo, R., et al. 2021, *A&A*, 645, A96
- Pepe, F., Mayor, M., Rupprecht, G., et al. 2002, *The Messenger*, 110, 9
- Pollacco, D. L., Skillen, I., Collier Cameron, A., et al. 2006, *PASP*, 118, 1407
- Queloz, D., Bouchy, F., Moutou, C., et al. 2009, *A&A*, 506, 303
- Queloz, D., Mayor, M., Udry, S., et al. 2001, *The Messenger*, 105, 1
- Rajpaul, V., Aigrain, S., Osborne, M. A., Reece, S., & Roberts, S. 2015, *MNRAS*, 452, 2269
- Rasio, F. A. & Ford, E. B. 1996, *Science*, 274, 954
- Ricker, G. R., Winn, J. N., Vanderspek, R., et al. 2015, *Journal of Astronomical Telescopes, Instruments, and Systems*, 1, 014003
- Roberts, S., Osborne, M., Ebdon, M., et al. 2013, *Philosophical Transactions of the Royal Society of London Series A*, 371, 20110550
- Rosenthal, L. J., Knutson, H. A., Chachan, Y., et al. 2022, *ApJS*, 262, 1
- Rossiter, R. A. 1924, *ApJ*, 60, 15
- Santos, N. C., Santerne, A., Faria, J. P., et al. 2016, *A&A*, 592, A13
- Santos, N. C., Sousa, S. G., Mortier, A., et al. 2013, *A&A*, 556, A150
- Scargle, J. D. 1982, *ApJ*, 263, 835
- Schlafly, E. F. & Finkbeiner, D. P. 2011, *ApJ*, 737, 103
- Ségransan, D., Udry, S., Mayor, M., et al. 2010, *A&A*, 511, A45
- Sha, L., Vanderburg, A. M., Huang, C. X., et al. 2022, *arXiv e-prints*, arXiv:2209.14396
- Skrutskie, M. F., Cutri, R. M., Stiening, R., et al. 2006, *AJ*, 131, 1163
- Smith, J. C., Stumpe, M. C., Van Cleve, J. E., et al. 2012, *PASP*, 124, 1000
- Snedden, C. A. 1973, PhD thesis, THE UNIVERSITY OF TEXAS AT AUSTIN.
- Snellen, I. A. G. & Brown, A. G. A. 2018, *Nature Astronomy*, 2, 883
- Sousa, S. G. 2014, [arXiv:1407.5817] [arXiv:1407.5817]
- Sousa, S. G., Santos, N. C., Adibekyan, V., Delgado-Mena, E., & Israelian, G. 2015, *A&A*, 577, A67
- Speagle, J. S. 2019, *arXiv e-prints*, arXiv:1909.12313
- Stassun, K. G., Oelkers, R. J., Paegert, M., et al. 2019, *AJ*, 158, 138
- Stassun, K. G., Oelkers, R. J., Pepper, J., et al. 2018, *AJ*, 156, 102
- Steffen, J. H., Ragozzine, D., Fabrycky, D. C., et al. 2012, *Proceedings of the National Academy of Science*, 109, 7982
- Stumpe, M. C., Smith, J. C., Catanzarite, J. H., et al. 2014, *PASP*, 126, 100
- Stumpe, M. C., Smith, J. C., Van Cleve, J. E., et al. 2012, *PASP*, 124, 985
- Suárez Mascareño, A., Rebolo, R., González Hernández, J. I., & Esposito, M. 2015, *MNRAS*, 452, 2745
- Thorngren, D. P., Fortney, J. J., Murray-Clay, R. A., & Lopez, E. D. 2016, *ApJ*, 831, 64
- Tokovinin, A. 2018, *PASP*, 130, 035002
- Wang, X.-Y., Wang, Y.-H., Wang, S., et al. 2021, *ApJS*, 255, 15
- Ward, W. R. 1997, *Icarus*, 126, 261
- Weidenschilling, S. J. & Marzari, F. 1996, *Nature*, 384, 619
- Weiss, L. M., Fabrycky, D. C., Agol, E., et al. 2020, *AJ*, 159, 242
- Weiss, L. M., Marcy, G. W., Rowe, J. F., et al. 2013, *ApJ*, 768, 14
- Winn, J. N. 2010, *arXiv e-prints*, arXiv:1001.2010
- Wright, E. L., Eisenhardt, P. R. M., Mainzer, A. K., et al. 2010, *AJ*, 140, 1868
- Wright, J. T., Upadhyay, S., Marcy, G. W., et al. 2009, *ApJ*, 693, 1084
- Wu, D.-H., Rice, M., & Wang, S. 2023, *AJ*, 165, 171
- Wu, Y. & Murray, N. 2003, *ApJ*, 589, 605
- Zechmeister, M. & Kürster, M. 2009, *A&A*, 496, 577
- Zhu, W. 2023, *arXiv e-prints*, arXiv:2306.16691
- Zhu, W., Dai, F., & Masuda, K. 2018, *Research Notes of the American Astronomical Society*, 2, 160
- Zhu, W. & Wu, Y. 2018, *AJ*, 156, 92

**Table A.1.** WASP-132 CORALIE 07 RVs.

CORALIE07		
BJD	RV [ $\text{m s}^{-1}$ ]	RV error [ $\text{m s}^{-1}$ ]
2456717.73665239	31104.7	11.7
2456749.88330616	30997.6	12.5
2456772.83833124	31000.8	11.3
2456779.80482489	31004.5	14.9
2456781.68823019	31090.7	13.0
2456782.75296464	31105.1	12.2
2456803.73759273	31066.3	26.6
2456808.75158589	31033.0	18.1
2456810.73750268	31055.3	17.3
2456811.69973084	31025.9	15.1
2456813.73159885	30990.5	32.2
2456814.74102061	30968.2	16.0
2456830.68796066	31018.8	16.0
2456833.58020731 <sup>b</sup>	31036.7	15.2
2456840.60592619	31022.7	22.6
2456853.53751253	31124.8	57.3
2456855.61273790	30985.8	14.6
2456856.59422537	30976.7	12.0
2456880.53254910	31024.8	17.3
2456888.54232948	31037.3	15.1
2456889.52621581	31042.7	12.4
2456910.48465720	31046.2	25.5

<sup>b</sup> RV during transit of planet b.

## Appendix A: Supplementary material

**Table A.2.** WASP-132 CORALIE 14 RVs.

CORALIE14		
BJD	RV [ $\text{m s}^{-1}$ ]	RV error [ $\text{m s}^{-1}$ ]
2457031.85994539	31006.8	19.0
2457072.87336473	30979.1	14.7
2457085.80107186	30883.2	16.0
2457086.74260622	30907.8	16.4
2457111.67974096	30951.1	22.4
2457112.85851323	30933.3	39.7
2457114.83854385	30931.0	27.8
2457139.68574167	30995.5	24.7
2457194.67667381	30964.5	32.2
2457405.83694040	30905.9	15.1
2457412.84526021	30889.0	20.6
2457426.84822632	30933.5	11.8
2457428.82227642	30951.0	9.5
2457455.88963994	30913.0	14.6
2457484.75663684	30930.1	12.4
2457548.66992385	30973.7	13.4
2457807.78940591	31107.7	14.8
2457814.86410615	31118.9	10.2
2457850.62687922	31139.1	21.0
2457890.60954413	31084.6	17.9
2457949.57446668	31119.2	18.1
2458168.86611666	31162.7	15.8
2458205.83637135	31167.4	14.4
2458537.70831475	31173.0	32.4
2458576.85512151	31139.1	30.5
2458635.73804677	31220.2	29.6
2458637.56054081	31204.8	22.1
2458639.61313859	31125.5	23.8
2458890.77020664	30988.1	35.0
2459250.79901148	31123.7	51.3
2459264.82234224	31148.6	38.4
2459267.80057266	31072.1	31.9
2459270.82059757	31146.8	36.6
2459313.76439322 <sup>c</sup>	31178.0	37.2
2459343.74796327	31151.8	87.5
2459374.65916209	31085.4	30.3
2459421.52299861	31206.9	38.7
2459441.50598573	31207.4	93.0
2459460.48774659	31132.2	39.8
2459585.84591729 <sup>c</sup>	31257.1	30.4
2459620.80145690	31316.3	29.1
2459624.78262691	31180.9	27.2
2459648.74828436	31285.9	17.9
2459689.67318548	31194.9	27.4
2459703.67734296	31177.0	17.8
2459724.77238650	31202.7	21.9
2459750.65927053	31298.9	35.7
2459996.88794484	31294.3	37.2
2460011.89698716	31266.4	35.7
2460017.79286637 <sup>c</sup>	31258.4	24.2
2460030.85902694	31282.8	29.7

<sup>c</sup> RV during transit of planet c.

**Table A.3.** Radial velocities of WASP-132 from the HARPS spectrograph.

HARPS				
BJD	RV [m s <sup>-1</sup> ]	CCF FWHM	CCF BIS	S <sub>MW</sub>
2459596.85359639	31196.51±4.16	6487.05±9.17	52.44±5.89	0.677±0.037
2459600.82703273	31297.07±2.85	6449.48±9.12	46.93±4.03	0.569±0.024
2459601.84852919	31258.97±2.31	6448.61±9.12	36.13±3.26	0.597±0.018
2459602.81320430	31225.86±2.23	6452.16±9.12	33.05±3.15	0.447±0.018
2459609.81546504	31224.31±1.97	6433.56±9.10	50.59±2.79	0.500±0.015
2459610.86107604	31215.37±2.18	6435.05±9.10	43.47±3.08	0.560±0.016
2459620.86536289	31350.87±2.32	6516.31±9.22	52.84±3.28	0.575±0.018
2459622.88504200 <sup>b</sup>	31299.46±2.03	6522.54±9.22	58.51±2.87	0.581±0.014
2459625.88370669	31253.67±2.69	6494.66±9.18	65.60±3.80	0.620±0.021
2459629.85577601 <sup>b</sup>	31282.68±1.66	6450.51±9.12	56.82±2.34	0.509±0.010
2459643.73761137	31307.98±1.83	6422.76±9.08	40.31±2.59	0.486±0.013
2459643.84851150	31299.31±1.71	6428.69±9.09	34.09±2.42	0.555±0.011
2459644.73713595	31270.04±2.23	6431.54±9.10	35.84±3.16	0.560±0.017
2459645.75462429	31240.82±2.19	6448.64±9.12	28.16±3.10	0.594±0.016
2459645.87966891	31244.74±2.04	6446.53±9.12	31.51±2.89	0.604±0.016
2459646.71633210	31248.37±1.97	6467.56±9.15	33.86±2.79	0.610±0.014
2459646.84188594	31254.62±2.17	6471.90±9.15	33.69±3.06	0.596±0.015
2459647.72550826	31286.24±2.10	6490.41±9.18	36.52±2.97	0.607±0.015
2459647.83792441	31290.56±1.87	6478.46±9.16	33.48±2.65	0.594±0.012
2459648.75634046	31333.46±1.86	6496.41±9.19	42.12±2.63	0.612±0.012
2459648.84720395	31334.86±1.85	6498.47±9.19	36.27±2.62	0.589±0.013
2459657.81727319	31318.92±2.72	6484.60±9.17	40.04±3.85	0.617±0.018
2459658.77261715 <sup>b</sup>	31279.04±2.04	6473.09±9.15	61.21±2.89	0.591±0.013
2459658.89763733	31270.00±2.27	6474.67±9.16	56.16±3.21	0.591±0.020
2459659.70831774 <sup>c</sup>	31233.01±2.10	6460.12±9.14	53.86±2.98	0.612±0.014
2459659.89182556	31226.17±2.29	6451.25±9.12	45.58±3.23	0.587±0.021
2459660.71693905 <sup>c</sup>	31227.97±1.84	6439.33±9.11	56.90±2.60	0.567±0.012
2459660.89390691	31228.32±2.44	6429.28±9.09	58.93±3.45	0.530±0.022
2459661.67725759	31257.62±2.79	6439.97±9.11	58.97±3.95	0.544±0.022
2459661.83249932	31266.74±2.38	6429.74±9.09	56.49±3.37	0.520±0.018
2459662.81585070	31310.29±2.63	6420.12±9.08	42.22±3.72	0.595±0.019
2459662.89068195	31307.92±3.42	6425.04±9.09	41.54±4.84	0.530±0.032
2459663.80633121	31342.73±2.20	6436.77±9.10	34.27±3.11	0.553±0.014
2459663.90930075	31336.83±2.68	6434.25±9.10	31.42±3.79	0.567±0.029
2459664.72035913 <sup>c</sup>	31335.78±2.18	6438.80±9.11	27.44±3.08	0.562±0.014
2459664.89978015	31330.18±2.43	6444.92±9.11	41.82±3.44	0.575±0.024
2459665.65194515 <sup>b</sup>	31306.60±1.89	6450.70±9.12	35.81±2.68	0.503±0.013
2459665.86529170 <sup>b</sup>	31291.63±2.13	6439.30±9.11	22.27±3.02	0.487±0.019
2459666.66549127	31265.46±2.01	6440.28±9.11	41.85±2.85	0.535±0.015
2459666.84245806	31250.20±2.14	6445.55±9.12	36.33±3.03	0.523±0.017
2459667.68264761	31244.12±2.35	6448.39±9.12	33.90±3.32	0.499±0.018
2459667.83604799	31246.16±2.03	6453.90±9.13	40.58±2.87	0.512±0.016
2459668.69320521	31266.67±2.52	6473.86±9.16	44.27±3.56	0.471±0.018
2459668.87707016	31270.77±2.99	6456.83±9.13	43.51±4.23	0.486±0.030
2459669.69259204	31311.84±1.95	6455.27±9.13	51.46±2.75	0.530±0.012
2459669.88676987	31312.32±2.37	6451.82±9.12	52.16±3.35	0.531±0.023
2459670.67122426	31341.59±2.16	6465.36±9.14	53.75±3.06	0.503±0.016
2459670.80690321 <sup>c</sup>	31331.27±3.93	6469.06±9.15	39.21±5.56	0.536±0.036

<sup>b</sup> RV during transit of planet b.<sup>c</sup> RV during transit of planet c.

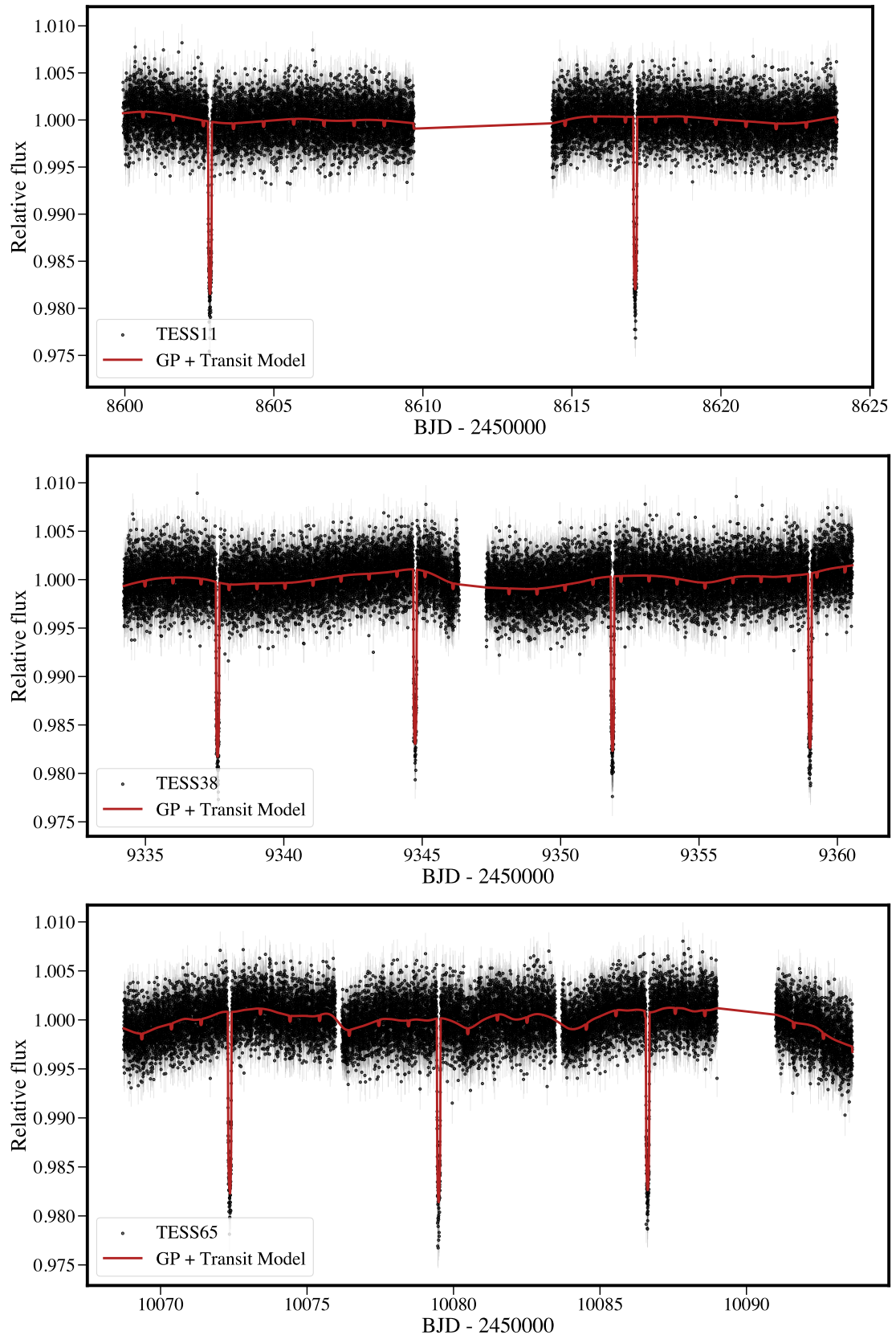


**Fig. A.1.** TESS Sectors 11, 38, and 65 with the GP and transit model of both WASP-132 b and WASP-132 c from `juliet` as described in Section 3.3.

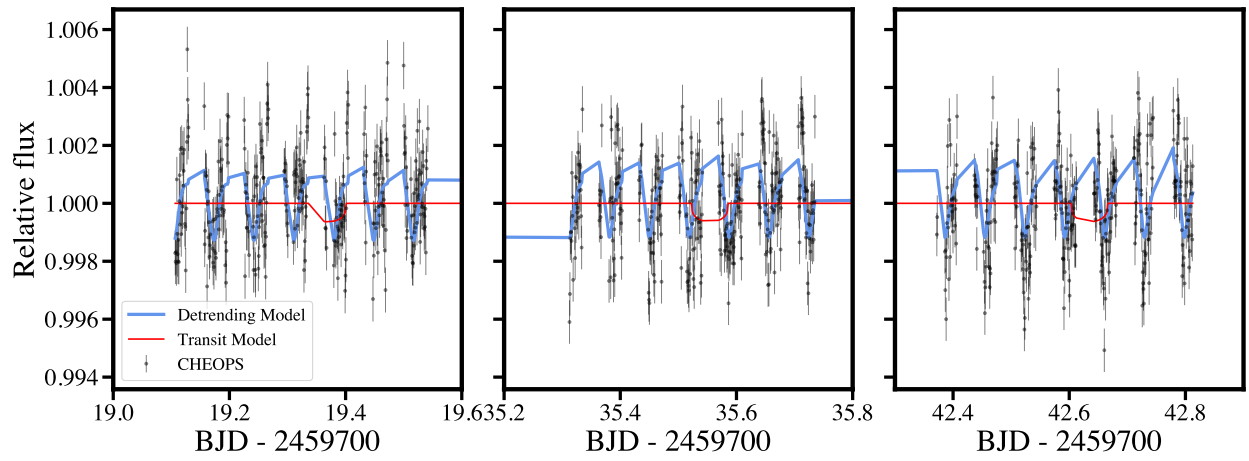


**Fig. A.2.** CHEOPS data of WASP-132 with the transit model of WASP-132 c and the detrending model that is detrended with the background flux and the roll angle  $\phi$  by using  $\cos(\phi)$ ,  $\cos(2\phi)$ ,  $\sin(\phi)$ , and  $\sin(2\phi)$  with `juliet` as described in Section 3.3.